Petrology of metapelites in the Bugaboo aureole, British Columbia, Canada

D. R. M. PATTISON AND C. L. DEBUHR
Department of Geoscience, University of Calgary, Calgary, AB T2N 1N4, Canada (pattison@ucalgary.ca)

ABSTRACT   Contact metamorphism of greenschist facies Neoproterozoic turbidites by the Cretaceous Bugaboo Batholith in southeastern British Columbia has resulted in a well-developed contact aureole. The aureole is about 1 km wide and can be divided into three main zones: (i) spotted phyllite zone, extending from the first appearance of spots of cordierite or andalusite to the last occurrence of primary chlorite; (ii) cordierite + andalusite + biotite zone, comprising hornfelses or schists with abundant porphyroblasts of cordierite and andalusite and, at higher grades, fibrolitic sillimanite; and (iii) K-feldspar zone, characterized by hornfelses and schists that, in the inner part of this zone, are variably migmatitic. Four parts of the aureole were examined, three of which are characterized by schists, and one of which (Cobalt Lake area) is characterized by hornfelses and has exceptional exposure and comparatively unaltered rocks. Petrographic, modal, mineral-compositional and whole rock-compositional data were collected from the Cobalt Lake transect, allowing the prograde reaction sequence to be inferred. Notable features of the aureole at Cobalt Lake include: initial development of andalusite and plagioclase at the expense of paragonite-rich white mica; a narrow interval across which cordierite, andalusite and biotite increase markedly at the expense of chlorite; gradual development of andalusite and biotite at the expense of cordierite and muscovite upgrade of chlorite consumption; and near-simultaneous development of andalusite + K-feldspar and sillimanite, the latter indicating a pressure of contact metamorphism of ~3 kbar. In other parts of the aureole, the development of sillimanite downgrade of the initial development of K-feldspar suggests slightly higher pressures of contact metamorphism. Lack of correspondence between the observed sequence of reactions in the aureole and those predicted thermodynamically suggests that modifications to some of the thermodynamic data or activity–composition models may be required. Textural features in the aureole suggest the influence of kinetic factors on metamorphic recrystallization, including: (i) deformation-catalysed reaction in the schists compared to the hornfelses, as indicated by different mineral-growth sequences inferred from microstructures, and (ii) heating rate-controlled recrystallization, as indicated by the decrease in grain size of hornfelses with increasing metamorphic grade.

Key words: contact metamorphism; kinetics; metapelites; phase equilibria; thermodynamics.

INTRODUCTION

Contact aureoles around igneous intrusions, although spatially limited and reflective of local rather than regional processes, have nevertheless been of great utility to the development of concepts and techniques of metamorphic petrology (e.g. Kerrick, 1991). Most aureoles record metamorphism at low pressures (<~4 kbar), and represent relatively simple metamorphic settings in which the direction of increasing grade is clear and the metamorphic cycle of heating and cooling takes place more rapidly than in regional terranes. For these reasons, they have been particularly useful in constraining low-pressure phase metapelitic equilibria that are difficult to model thermodynamically (e.g. Pattison & Tracy, 1991). Concerning the latter, subsolidus phase equilibria involving the characteristic low-*P* porphyroblastic mineral cordierite continue to be

problematic to model (e.g. Pattison *et al.*, 2002; White *et al.*, 2014).

This study describes a well-exposed, cordierite-bearing contact aureole surrounding the Cretaceous Bugaboo Batholith in southeast British Columbia. Petrographic, modal, mineral chemical and whole rock-compositional data are used to infer the prograde reaction sequence in the aureole, which in turn is used to evaluate thermodynamic models of low-*P* metapelitic phase equilibria. In addition to the phase equilibrium aspects, there are a number of textural features in the rocks that indicate the influence of kinetic factors on the development of the mineral assemblages.

LOCATION AND REGIONAL GEOLOGY

The Bugaboo Batholith and aureole are located in the Lardeau map area in southeastern British Colum-

bia, ~30 km west of the town of Radium (Fig. 1a). The Batholith is emplaced in turbiditic strata of the Horsethief Creek Group, part of the Neoproterozoic Windermere Supergroup (Reesor, 1973). The Batholith is located in the axial zone of the Purcell Anticlinorium, a Mesozoic, regional-scale, NW-trending fold belt with an overall anticlinorial geometry. The regional structures in the vicinity of the intrusion comprise moderate to tight, upright, NW-trending, gently NW-plunging folds. A prominent NW-trending, steeply dipping cleavage in the pelites and semipelites is axial planar to the folds. Later crenulations variably overprint the cleavage. The Batholith is emplaced within the chlorite zone of a regional Barrovian metamorphic sequence (Fig. 1a).

THE BUGABOO BATHOLITH AND ITS STRUCTURAL AUREOLE

The Bugaboo Batholith is exposed over ~100 km^2 and consists of two main phases: a hornblende + biotite granodiorite in the west, and a biotite granite/ quartz monzonite in the east (Reesor, 1973) (Fig. 1b). Rb–Sr whole rock plus apatite isochron analysis of the biotite granite gave an age of 107 ± 1 Ma (Brandon, 1992). K–Ar dating of biotite (Archibald et al., 1984) gave cooling ages of 89 ± 2 and 94 ± 2 Ma for the granodiorite and granite, respectively, although field evidence suggests that the granodiorite is older (Reesor, 1973).

In addition to the contact metamorphic aureole that is the focus of this paper, the Bugaboo Batholith is surrounded by a 'structural aureole', a term coined by Reesor (1973) to describe a variety of structural effects related to emplacement of the intrusion that extend up to 5 km from the intrusive contacts. These include re-orientation of regional folds, from shallowly NW- or SE-plunging to steeply plunging, and development of contact-parallel foliations and crenulations of the regional cleavage, both of which become more pronounced as the contact is approached. The effects are most noticeable where the regional structures trend at a high angle to the intrusive contact. Where the contact is approximately parallel to the strike of the regional structures, there is no evidence for reorientation of the regional structures, although a tightening of these cannot be ruled out. The present-day widths of the metamorphic zones described below may have been affected by the emplacement-related strain.

THE BUGABOO AUREOLE

The Bugaboo aureole is ~1 km wide, based on the outermost development of 'spots' of cordierite or andalusite. The aureole is divided into three main zones (Fig. 1b). The outer zone (Zone 1) extends from the first appearance of spots of cordierite or andalusite to the last occurrence of primary chlorite. The rocks largely retain the phyllitic texture of the regional host rocks, giving rise to the term 'spotted phyllite zone'. The middle zone (Zone 2) comprises hornfelses or schists with abundant porphyroblasts of cordierite and andalusite and, at higher grades, sparse fibrolitic sillimanite. The inner zone (Zone 3) extends from the first development of metamorphic K-feldspar to the igneous contact, and is characterized by dark hornfelses and schists that, in the inner part of this zone, are variably migmatitic. These broad zones are divided into subzones described below.

Four parts of the aureole were examined (Fig. 1b). The Cobalt Lake area is dominated by porphyroblas-
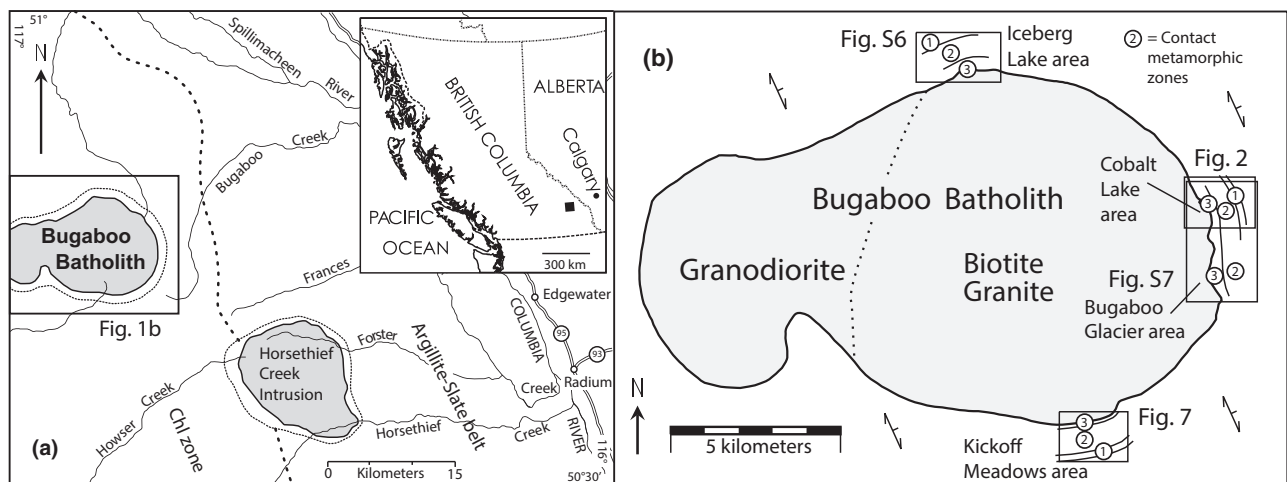
Fig. 1. (a) Location of Bugaboo Batholith in southeastern British Columbia (from Reesor, 1973). (b) Location of parts of aureole examined. The numbered metamorphic zones are described in the text. Structural symbols show trend of regional bedding and cleavage.

tic hornfelses. Because of excellent exposure, relatively unaltered rocks and relative ease of access, this area was examined in most detail (field observations, petrography, modal mineralogy, whole rock and mineral chemistry, petrogenetic modelling). The Kickoff Meadows, Iceberg Lake and Bugaboo Glacier areas are dominated by schists rather than hornfelses. The schists are more altered than the hornfelses at Cobalt Lake, so observations in these areas were restricted to the field and petrography.

Cobalt Lake area

In the Cobalt Lake area (Figs 1b & 2), the intrusive contact strikes parallel to the regional structural trends and dips outwards, beneath the host metasedimentary rocks, at ~60–65° (Figs 2c & S3). Structures in the host metasedimentary rocks include NW-trending, shallowly NW- or SE-plunging folds and a steeply NE-dipping axial planar cleavage (Figs S1 & S3), indistinguishable from regional structures but possibly tightened. Pegmatitic and aplitic dykes and sills intrude the metasedimentary host rocks within ~200 m of the contacts. The pegmatites contain muscovite, tourmaline and rarely beryl, whereas the aplites contain muscovite and rarely garnet.

Figure 2 shows a metamorphic map of the Cobalt Lake area, simplified from the detailed mineral assemblage map in Fig. S2. The approximate dip of the isograds is shown in the cross-section in Fig. S3, based on the trend of isograds across topography, with the exception of the high-grade isograds which were assumed to be parallel to the exposed contact. The types and numbers of mineral assemblages as a function of distance from the contact are given in Table S1 (210 samples examined). Modal data for 33 selected samples are given in Table S2 and some key whole-rock and mineral chemical parameters for 24 minimally altered samples are given in Table S3. The data summarized in Table S3 are extracted from complete chemical analyses in Tables S4–S12 (comprising, respectively, whole rock, biotite, white mica, cordierite, andalusite, chlorite, plagioclase, K-feldspar and ilmenite analyses).

Regional grade phyllites

The regional pelitic host rocks are greenish, silvery-grey phyllites with a well-developed penetrative cleavage and variable later, overprinting crenulations (Fig. 3a). The phyllites contain the mineral assemblage Ms + Chl + Qtz + Ilm (abbreviations of Kretz, 1983), with variable amounts of either albitic plagioclase (interpreted to be altered detrital plagioclase) or paragonite-rich white mica, the latter intergrown with the more abundant muscovite (Fig. 3b). Paragonite could only be identified by combined back-scattered electron imaging and X-ray mapping (Fig. 3b). Chlorite occurs as either fine tabular grains intergrown

with muscovite in the matrix (Fig. 3b) or as more discrete, equant, rounded grains intergrown with muscovite. Other minerals of minor modal abundance variably present in the rocks include tourmaline, rutile, zircon, apatite, monazite, allanite and various sulphide minerals.

Zone 1a: Spotted phyllite zone (1030–870 m)

The first development of porphyroblasts ('spots') of cordierite or andalusite occurs ~1 km from the igneous contact (Fig. 2a). Rocks from this zone contain cordierite, andalusite, cordierite + andalusite or neither (Table S1), suggestive of bulk compositional control. Cordierite occurs as mm-size, light-coloured, equant, rounded spots on cleavage surfaces (Fig. 3c) that in thin section are altered to muscovite-rich intergrowths of matrix minerals (Fig. 3e). Andalusite occurs in mm-size, grey, elongate grains on cleavage surfaces that increase in grain size as grade increases (Fig. 3d). In many samples, the andalusite is packed with tiny inclusions (Fig. 3e), whereas in others it is relatively inclusion-free (Fig. 3f).

Pale, sub-mm porphyroblasts of plagioclase commonly occur in andalusite-bearing phyllites (Figs 3e,f & 4c). The plagioclase porphyroblasts are zoned (Fig. 3f), ranging most commonly from $X_{An} = 25$–35 in the cores to $X_{An} = 3$–23 in the rims (Tables S3 & S10). Biotite is a rare, modally minor, additional mineral restricted to a few cordierite-bearing samples. Upgrade of the spots-in isograd, but still within Zone 1a, the rocks progressively change from spotted phyllites to more silvery, knotted, fine-grained schists (cf. Fig. 3c,d).

Zone 1b: And–Crd–Bt–Chl zone (870–820 m)

About 160 m upgrade of the spots-in isograd, tiny, sub-mm, black porphyroblasts of biotite become visible in the knotted phyllites, marking the outer edge of the And–Crd–Bt–Chl zone. Over a short-distance (<50 m) upgrade of the first appearance of biotite, the rocks lose primary chlorite and change to densely porphyroblastic hornfelses (Fig. 4a). In addition to conspicuous cordierite, andalusite and biotite porphyroblasts, many samples contain sub-mm plagioclase porphyroblasts like those described in Zone 1a (Fig. 4c).

Zone 2a: And–Crd–Bt hornfels zone (820–300 m)

Zone 2a, the widest individual zone in the aureole at 520 m, is characterized by chlorite-free Crd + And + Bt hornfelses. Rocks at the outer edge of Zone 2a, and in the high-grade part of Zone 1a, show the coarsest porphyroblasts of andalusite and cordierite in the Cobalt Lake area, with individual porphyroblasts ranging up to 1 cm in their longest dimension (Fig. 4a). Reversely graded metamorphic layering, in which the darker, most
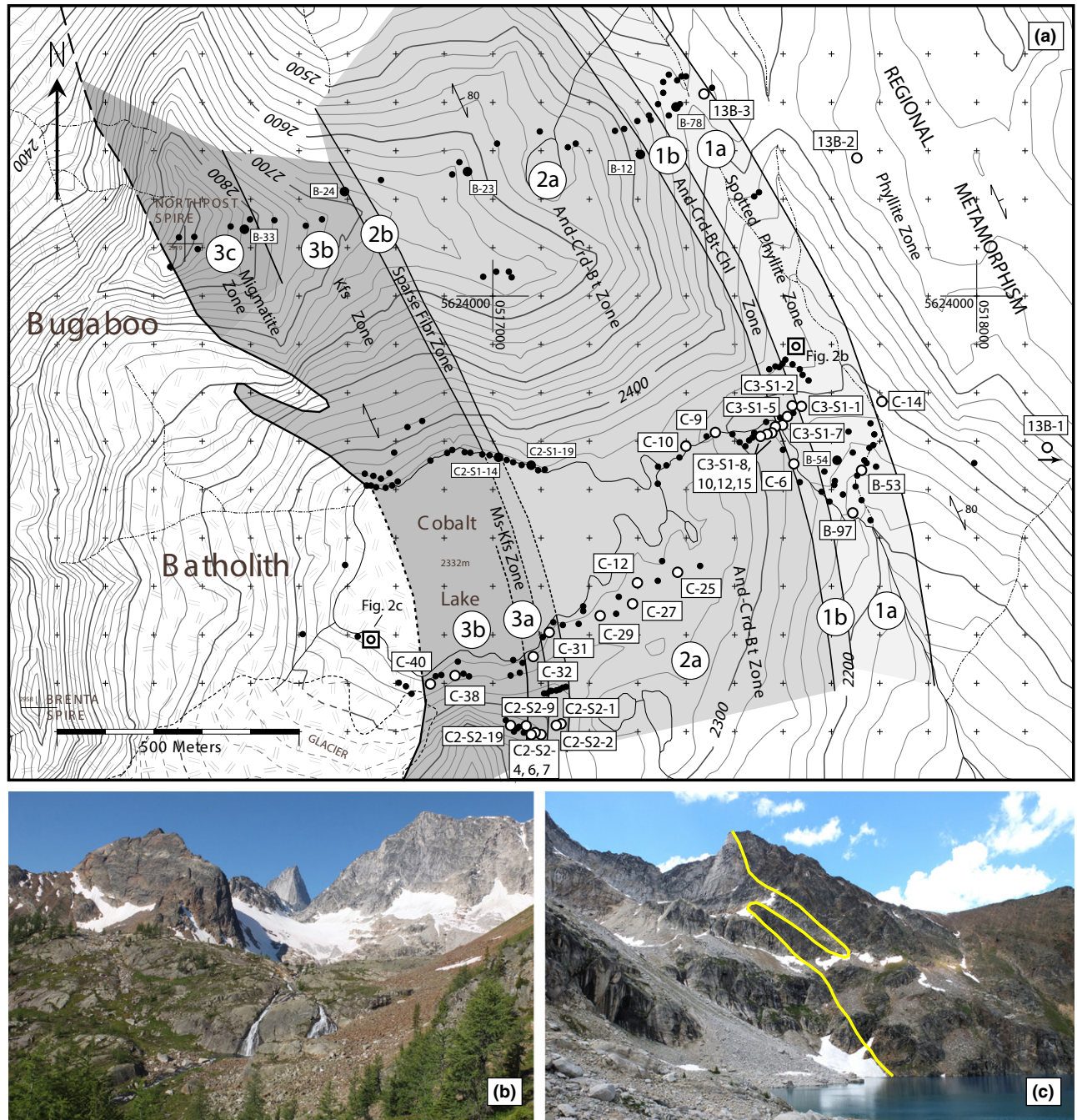
Fig. 2. (a) Map of metamorphic zones in the Cobalt Lake area, based on the detailed map of mineral assemblages in Fig. S2 (see Fig. 1b for location of area with respect to intrusion). UTM coordinates: NAD83. Numbered metamorphic zones are described in the text and summarized in Table S1. Small filled circles: sample locations. Larger filled circles with labels: samples for which photographs or photomicrographs provided in Figs 3–5. Open circles with labels: samples for which modal and/or chemical analyses performed. Circles in squares: location of sites from which photographs in (b, c) taken. Strike and dip symbol: representative orientation of foliation. Figures S1 and S3 show a structural map and cross-section, respectively, of the Cobalt Lake area. (b) Photograph looking upgrade across grey–brown outcrops and crags of contact metamorphosed pelitic hornfelses towards light-coloured cliffs of the Bugaboo granite above Cobalt Lake. Location of site from which photograph taken shown in (a). (c) Photograph showing the outwardly dipping intrusive contact, outlined in yellow, at the northwest end of Cobalt Lake. Location of site from which photograph taken shown in (a).

coarsely porphyroblastic portions correspond to what were originally fine-grained, muddy tops of individual turbidite layers, are common (Fig. 4d).

In thin section, cordierite, andalusite, biotite and locally plagioclase porphyroblasts grow across the foliated, fine-grained muscovite-rich matrix, as
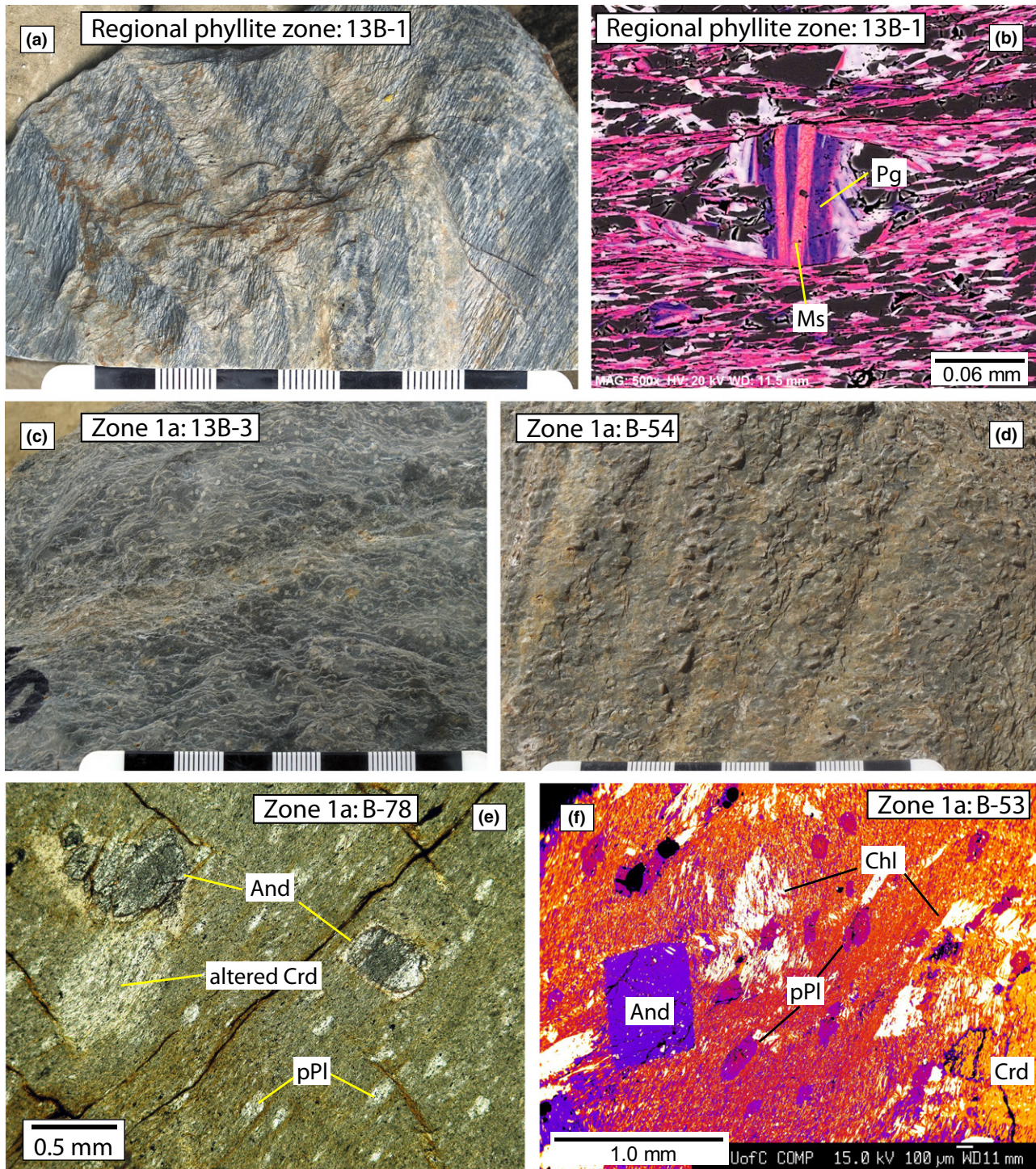
Fig. 3. Photographs and photomicrographs of regional grade host rocks and spotted phyllites from Zone 1 of aureole in Cobalt Lake area. Sample locations shown in Fig. 2a. Width of major divisions on scale bar: 1 cm. (a) Photograph of regional phyllite showing bedding and crenulated cleavage surfaces. (b) Grey-scale back-scattered electron (BSE) image of matrix of regional phyllite, with false-colour Na (purple) and K (pink) X-ray maps superimposed, highlighting occurrence of paragonite and muscovite, respectively. (c) Photograph of spotted phyllite from outer edge of Zone 1a. The small white spots are altered cordierite. (d) Photograph of porphyroblastic phyllite from upper part of Zone 1a, showing upward-weathering andalusite porphyroblasts. (e) Photomicrograph of spotted phyllite from upper part of Zone 1a showing: two inclusion-packed andalusite porphyroblasts partly altered to white mica at their rims; an altered cordierite porphyroblast; and numerous tiny porphyroblasts of plagioclase (pPl). (f) False colour BSE image of porphyroblastic phyllite from upper part of Zone 1a showing andalusite, cordierite and plagioclase porphyroblasts (pPl).

(a) Zone 2a: near C3-S1-8

(b) Zone 2a: B-12 — And, altered Crd, 0.5 mm

(c) And, Zone 2a: C3-S1-12, Bt, pPl, Crd, Crd, And, 1.0 mm

(d) Zone 2a: near C-10, 4 cm

(e) Zone 2a: near C-12

(f) Zone 2a: B-23, Bt, Crd, And, Bt, And, 0.7 mm

(g) Zone 2a: near C-29, Crd, And, 0.6 mm

(h) Bt, And, Fibr, Zone 2b: C2-S1-14, 0.1 mm
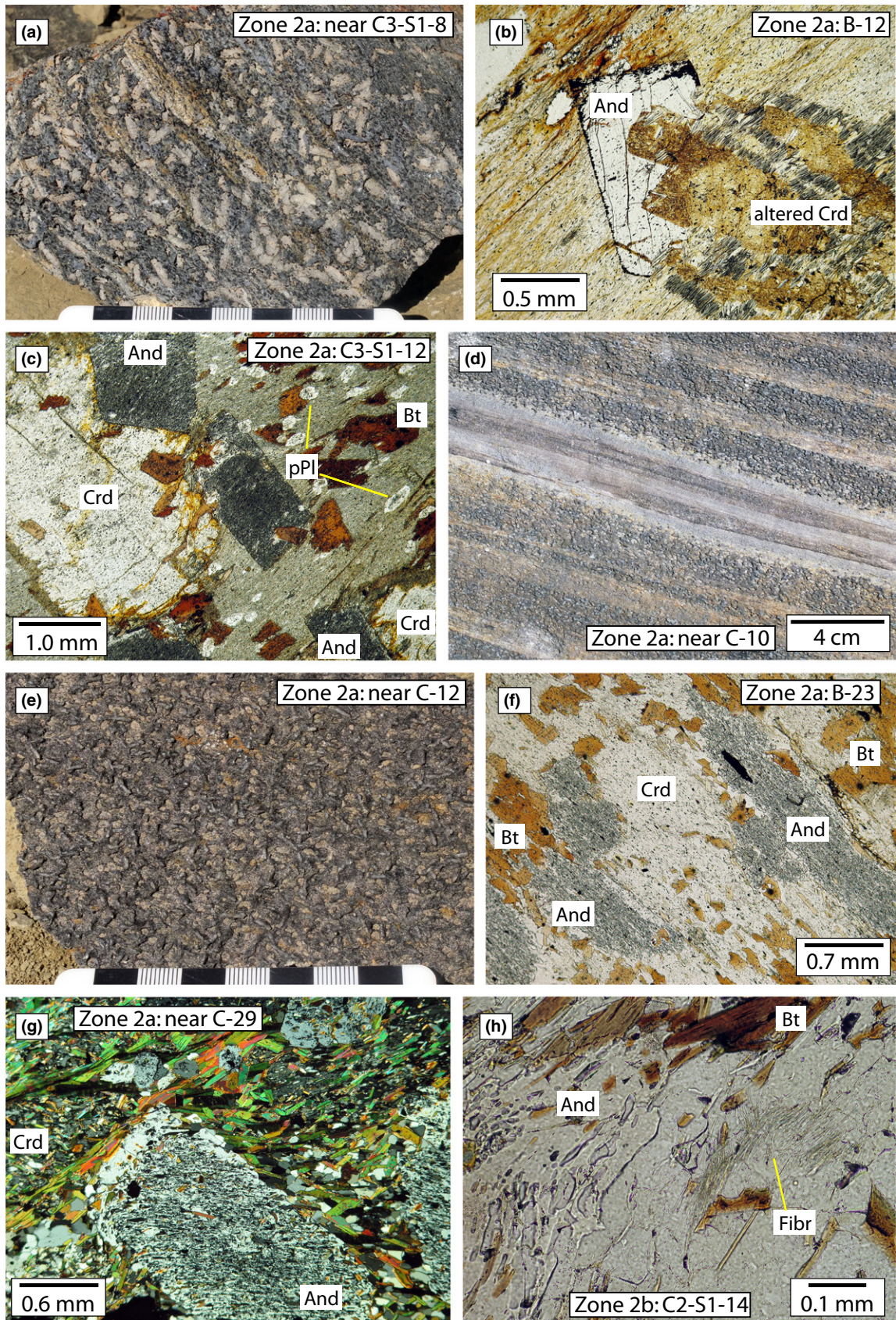
revealed by numerous fine-grained inclusions in the porphyroblasts whose orientation is continuous with the matrix fabric (Fig. 4b,c,f). Cordierite porphyroblasts most commonly have an ill-defined ovoid shape and are partially to wholly replaced by alteration products collectively known as 'pinite', ranging from brown, scaly, pseudo-isotropic products to fine-grained aggregates of muscovite and chlorite.

Andalusite porphyroblasts in most samples are inclusion-filled with an external habit ranging from prismatic to ovoid; in a few samples andalusite is inclusion-poor, idiomorphic and prismatic (Figs 3f & 4b), appearing as glassy grey grains in hand sample. Of the inclusion-rich andalusite grains, some contain central portions with a more densely packed, finer grained array of inclusions than the outer portions (Fig. 4c; and fig. 5c of Pattison *et al.*, 2002), suggestive of matrix coarsening between two stages of andalusite growth.

Andalusite and cordierite porphyroblasts show mutual inclusion and impingement relations (Fig. 4b, c,f). Inclusion-rich, andalusite porphyroblasts typically contain more abundant and coarser grained inclusions of quartz and other matrix minerals than cordierite (Fig. 4c,f). However, the centre-to-centre distances between inclusions in the cordierite and andalusite appear similar, and they define similar linear trends that are continuous with the matrix (Fig. 4c,f). These features suggest a period of broadly coeval growth of the two minerals. In a number of samples, especially those that are cordierite-rich, andalusite is restricted to anhedral, film-like growths between cordierite porphyroblasts (e.g. fig. 5e of Pattison *et al.*, 2002), indicating andalusite growth following cordierite growth.

The small plagioclase porphyroblasts first seen in Zone 1a occur as inclusions in all other porphyroblasts (Fig. 4c). Biotite occurs as discrete porphyroblasts, most commonly in the matrix, but sometimes as inclusions in andalusite and cordierite porphyroblasts (Fig. 4c,f; and fig. 5e of Pattison *et al.*, 2002).

At higher grade in Zone 2a, the average grain size of the porphyroblasts decreases (cf. Fig. 4a,e). The rocks become darker and more hornfelsic, reflecting in part a modal increase in biotite and decrease in muscovite. Muscovite in these rocks occurs as aligned grains in the matrix, interpreted to be primary, and as blocky, ragged grains with no preferred orientation, interpreted to be of retrograde origin, with both varieties present in some rocks. Biotite is finer grained and less porphyroblastic than at lower grade in Zone 2a, and is the main matrix mineral that defines the foliation (Fig. 4g; and fig. 5d of Pattison *et al.*, 2002). In the middle high-grade parts of Zone 2a, cordierite and andalusite crystals are typically wrapped by a weakly foliated biotite-rich matrix (Fig. 4g). Cordierite decreases in modal abundance compared to andalusite, and may appear somewhat corroded in thin section (Fig. 4g).

Andalusite develops a new texture in the middle high-grade parts of Zone 2a: thin, clear, relatively inclusion-poor overgrowths on the outsides of inclusion-rich andalusite crystals. These rims grow across the foliated biotite-rich matrix that itself wraps the inclusion-filled andalusite and cordierite crystals, and they locally envelop aligned crystals of the foliated matrix (Fig. 4g; and fig. 5d of Pattison *et al.*, 2002). The fine-grained inclusion trails in the inner portions of the andalusite crystals are commonly at an angle to the coarser grained enclosing foliated matrix, implying that matrix coarsening and matrix/porphyroblast reorientation occurred between the two stages of andalusite growth. Combined with the two stages of andalusite growth interpreted in some of

Fig. 4. Photographs and photomicrographs of hornfelses from Zone 2 of aureole in Cobalt Lake area. Sample locations shown in Fig. 2a. Width of major divisions on scale bar: 1 cm. (a) Photograph of coarsely porphyroblastic hornfels from outer edge of Zone 2a. Porphyroblasts of cordierite (light-coloured, downward-weathering shapes), andalusite (elongate grey prisms) and biotite (small black crystals) randomly overgrow relict bedding. (b) Photomicrograph of andalusite and altered cordierite from Zone 2a in which andalusite growth post-dated that of cordierite. (c) Photomicrograph of typical porphyroblastic hornfels from the outer edge of Zone 2a showing porphyroblasts of cordierite, andalusite, biotite and plagioclase (pPl) overgrowing a foliated, fine-grained micaceous matrix. Note: the inclusion-packed andalusite crystals; a large cordierite porphyroblast partly enveloping a pre-existing andalusite crystal (upper left); and the continuity of inclusion trails in the porphyroblasts with the external matrix fabric. (d) Photograph of outcrop surface from Zone 2a showing reverse (metamorphic) grading in contact metamorphosed turbidites. Individual graded layers have sharp lower and upper boundaries. Within each graded layer, light-coloured, non-porphyroblastic, quartz-rich metasandstone or metasiltstone grades upward into darker, more porphyroblastic hornfels. The porphyroblasts developed in what were originally the muddy tops of the graded turbidite layers. Stratigraphic way-up direction is to top of photograph. (e) Photograph of typical dark porphyroblastic hornfels from middle part of Zone 2a, showing small, downward weathering, ovoid cordierite porphyroblasts and upward-weathering, elongate andalusite prisms. Note the smaller size of porphyroblasts compared to those at the outer edge of Zone 2a, as shown in (a). (f) Photomicrograph of typical hornfels from middle of Zone 2a, showing inclusion-packed porphyroblasts of cordierite, andalusite and biotite; andalusite appears to envelop earlier formed cordierite. (g) Two generations of andalusite in hornfels from Zone 2a. Individual andalusite crystals contain an inner zone packed with fine-grained inclusions, and a clear, inclusion-poor outer rim. The outer rim overgrows a coarser grained, biotite-rich fabric that wraps cordierite and the inner inclusion-rich portions of the andalusite crystals. (h) Sparse fibrolitic sillimanite (fibrolite) in And + Crd + Bt hornfels from Zone 2c (cordierite not visible in field of view).
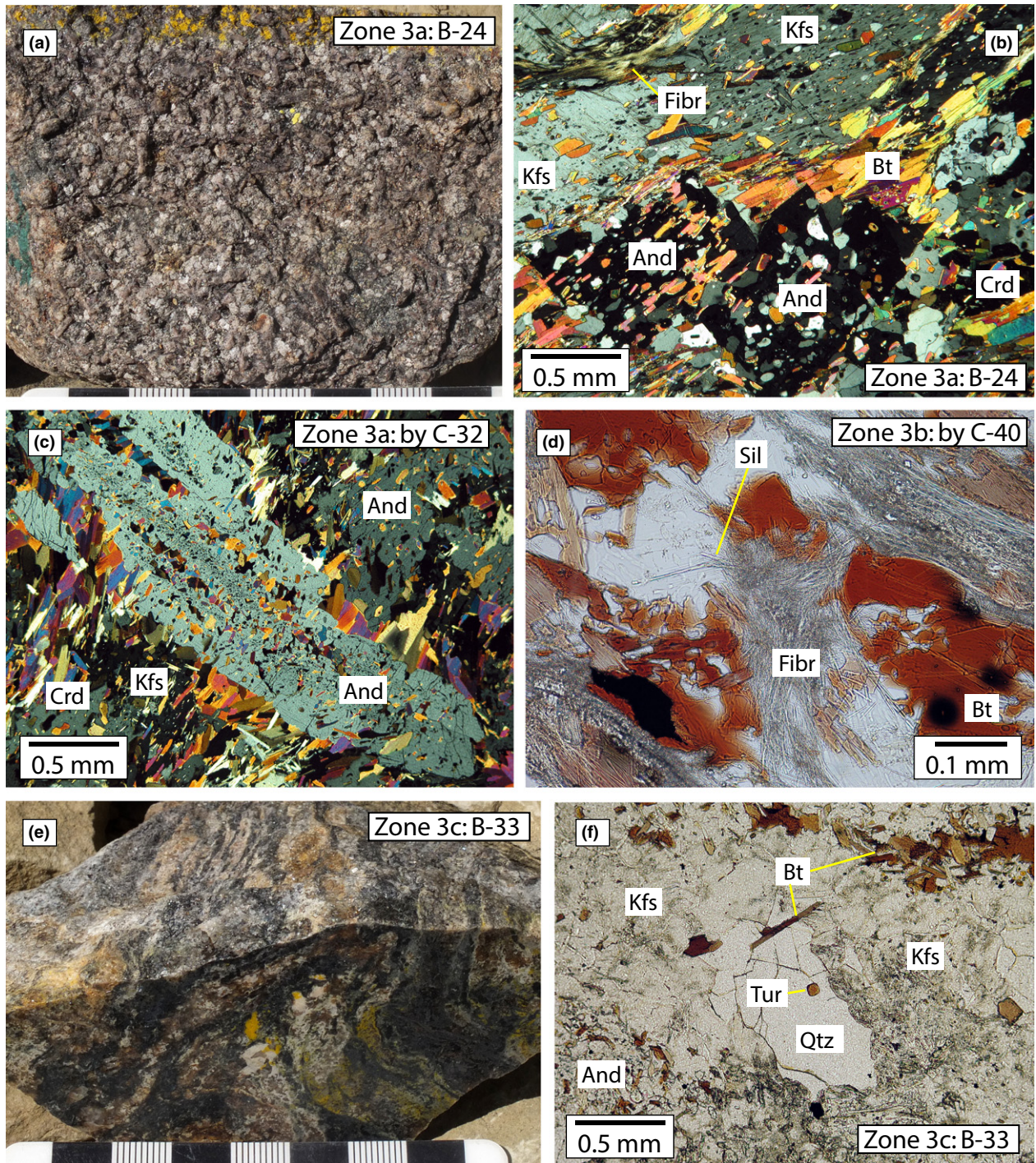
Fig. 5. Photographs and photomicrographs of hornfelses from Zone 3 of aureole in Cobalt Lake area. Sample locations shown in Fig. 2a. Width of major divisions on scale bar: 1 cm. (a) Photograph of K-feldspar-bearing hornfels from Zone 3a. Randomly oriented andalusite crystals show a dark core and lighter, sometimes pink, outer rim; K-feldspar occurs as discrete white grains, stained yellow at the top of the sample. (b) Photomicrograph of same sample as in (a), showing inclusion-filled K-feldspar porphyroblasts displaying cryptoperthitic exsolution, in addition to crystals of andalusite, cordierite, biotite and fibrolite. (c) Photomicrograph of K-feldspar-bearing hornfels from Zone 3a showing andalusite with inclusion-filled inner portion and inclusion-poor, idiomorphic outer portion. (d) Photomicrograph of a mass of fibrolite containing a few coarser crystals of sillimanite. (e) Photograph of ductilely deformed migmatite with quartzofeldspathic segregations. The cut surface has been stained with sodium cobaltinitrate to highlight K-feldspar (yellow) and plagioclase (white). (h) Photomicrograph of a quartzofeldspathic leucosome containing anhedral quartz and K-feldspar with minor biotite and tourmaline. The leucosome is contained in an andalusite-bearing host rock (see bottom), and has a biotite-rich selvage along its contact at the top of the photomicrograph.

the rocks in Zones 1b and 2a, the andalusite textures from the upper part of Zone 2a imply a third stage of andalusite growth.

Zone 2b: Sparse fibrolite zone (300–260 m)

Zone 2b is narrow (~40 m wide) and the rocks look the same in the field as those from the upper part of Zone 2a. Petrographic examination reveals the presence in some samples of sporadically developed, modally minor ($\ll$0.1 vol.%) bundles and aggregations of tiny (<1 μm wide), acicular crystals of sillimanite (Fig. 4h). Being <2 μm wide, this type of sillimanite classifies as fibrolite according to the criteria of Pattison (1992). The fibrolite occurs randomly in the rock, sometimes with a weak spatial association with biotite or coarse grains of quartz. Many samples from Zone 2b contain no fibrolite (Table S1).

Zone 3a: Muscovite–K-feldspar zone (260–210 m)

Approximately 260 m from the igneous contact, metamorphic K-feldspar first occurs, marking the low-grade boundary of Zone 3a. Zone 3a is characterized by the co-existence of K-feldspar and what is interpreted to be primary muscovite, based on the textural criteria noted above. K-feldspar is visible in the field as 1–2 mm, discrete, equant, white crystals (Fig. 5a). In thin section, the K-feldspar occurs as cryptoperthitic porphyroblasts full of inclusions (Fig. 5b). Many samples from Zone 3a do not contain K-feldspar (Table S1) and appear indistinguishable from the dark muscovite-poor or muscovite-absent hornfelses in Zones 2a and 2b. In contrast, a few very muscovite-rich, K-feldspar-absent samples occur in this narrow zone (Table S1).

Andalusite occurs as prismatic porphyroblasts that have a dark inner core and pale, sometimes pink, outer rim (Fig. 5a). Thin-section analysis (Fig. 5c) reveals that the dark inner portion consists of inclusion-rich andalusite like that seen in Zone 2, with the pale outer portion consisting of inclusion-poor, more idiomorphic andalusite that has overgrown a matrix fabric that is coarser grained than the fine inclusion array in the inner portions of the andalusite. The differences in this mantling relationship from the one described in the middle–upper grade parts of Zone 2 are that the width and colour contrast of the rim is greater, such that it is noticeable in the field, and it develops exclusively in samples that contain K-feldspar. Combined with the modal data, these textures suggest that andalusite grew in association with K-feldspar at the expense of muscovite, implying a fourth generation of andalusite growth in the aureole.

Fibrolite occurs in greater, but still minor (<0.1 vol.%), modal abundance in this zone compared to Zone 2b, and occurs in both K-feldspar-bearing and K-feldspar-absent rocks. It occurs in irregularly developed tufts and patches of hair-like crystals, most typically associated with quartz, biotite and less commonly K-feldspar (Fig. 5b,d). Rarely grains exceed 2 μm in width, indicative of sillimanite (Fig. 5d). In some samples, andalusite is incipiently replaced by fibrolite at corners, margins and along cracks, similar to the Kickoff Meadows area discussed below.

Zone 3b: K-feldspar zone (210–0 m)

This zone extends from the last occurrence of primary muscovite to the igneous contact. Most of the rocks from this zone are dark, biotite-rich hornfelses containing Crd + Bt + And + Sil, some with K-feldspar (Table S1). Cordierite is typically altered and in some samples develops a sub-idiomorphic, neoblastic habit suggestive of recrystallization; this texture occurs in samples with or without K-feldspar.

Zone 3c: Migmatite zone

Rocks with the overall appearance of anatectic migmatites are found in a few outcrops ~200 m from the intrusive contact near the summit of Northpost Spire, vertically above the outwardly dipping intrusive contact (Fig. 2a,c). These sparse outcrops give rise to an ill-defined migmatite zone. The migmatites contain mm–cm-scale leucocratic, quartzofeldspathic segregations and veins within more melanocratic domains, and show textures and structures indicative of ductile deformation (Fig. 5e). Microstructural features suggestive of an anatectic origin for the leucosomes include: coarse-grained segregations of anhedral, sometimes interstitial, quartz and either plagioclase or K-feldspar, mantled by biotite-rich selvages (Fig. 5e,f); and thin, undeformed biotite plates that are mutually included in adjacent quartz and K-feldspar grains, suggesting that the quartz and K-feldspar crystallized around them (Fig. 5f). Tourmaline may also be present. The anhedral K-feldspar in the leucosomes contrasts with the discrete, equant, inclusion-rich K-feldspar porphyroblasts in the non-migmatic hornfelses (cf. Fig. 5b,e).

Within Zone 3c, most of the outcrops are non-migmatitic, comprising dark hornfelses like those seen elsewhere in Zones 2 and 3. The mineral assemblages in the migmatite zone are the same as in the rest of Zone 3 (Table S1).

Kickoff Meadows area

The Kickoff Meadows area (Figs 1b & 6) is characterized by an ENE-trending intrusive contact that strikes at a high angle to the NNW-trending regional structures. The intrusive contact dips inward at ~70°, such that the host metasedimentary rocks are in the footwall. Within a few hundred metres of the contact, bedding, foliation (schistosity) and fold axes in the
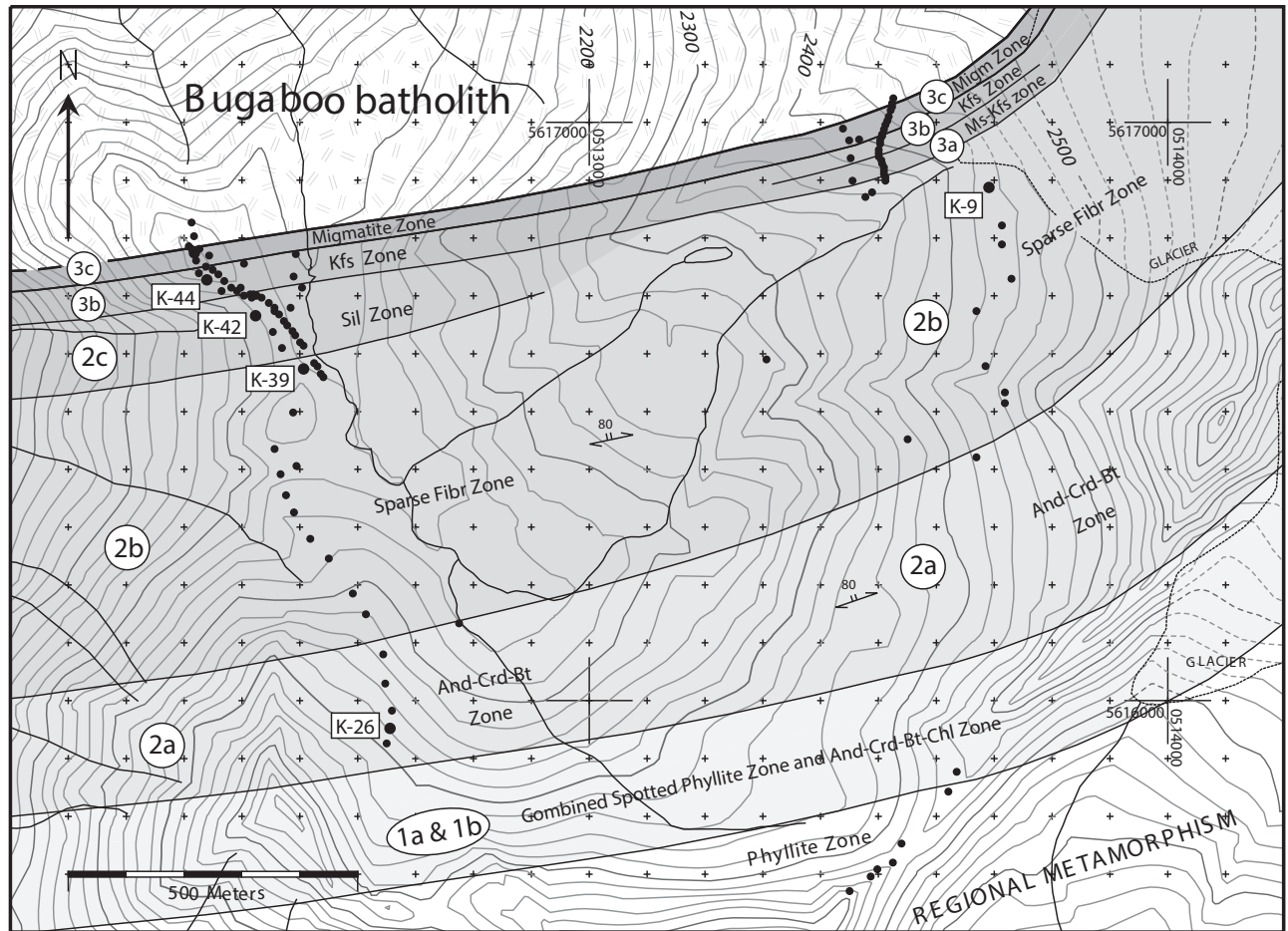
Fig. 6. Map of metamorphic zones in the Kickoff Meadows area, based on the detailed map of mineral assemblages in Fig. S5 (see Fig. 1b for location of area with respect to intrusion). UTM coordinates: NAD83. Figure S4 shows a structural map of the Kickoff meadows area. Numbered metamorphic zones are described in the text and summarized in Table S1. Small filled circles: sample locations. Larger filled circles with labels: samples for which photographs or photomicrographs are provided in Fig. 7. Strike and dip symbols: representative orientations of intrusion-related foliations.

metasedimentary rocks trend predominantly parallel to the contact (Fig. S4), as do pegmatite and aplite dykes where present. Moving away from the contact, the evidence of pre-existing regional structures increases; outside the visible contact aureole (~1200 m), the orientation of folds and foliations (cleavage) is intermediate between regional structures and those closer to the intrusion.

Figure 6 shows a metamorphic map of the Kickoff Meadows area, simplified from Fig. S5. Table S1 gives types and numbers of mineral assemblages as a function of distance from the contact (97 samples examined). The width of the contact aureole at Kickoff Meadows, as defined by the first occurrence of 'spots', is 1160 m, a little wider than at Cobalt Lake. In contrast to Cobalt Lake, the aureole rocks are schists rather than hornfelses (Fig. 7a), and they are typically more altered. Zones 1a and 1b are constrained to a width of 200–250 m, similar to Cobalt Lake, but are only represented by a single

sample of cordierite-spotted phyllite (Fig. 6; Table S1).

Zone 2a: And–Crd–Bt schist zone (950–730 m)

Zone 2a, defined by the occurrence of chlorite-free Crd + And + Bt mineral assemblages, is narrower at Kickoff Meadows than at Cobalt Lake (220 *v.* 520 m; Fig. 6). The schists contain a well-defined foliation defined by aligned muscovite and biotite; discrete biotite porphyroblasts are absent. Cordierite porphyroblasts (2–7 mm) are wrapped by this fabric and, where not altered, typically contain trails of fine-grained inclusions at a high angle to the enveloping, more coarse-grained, matrix (Fig. 7b,c).

In a few samples, andalusite porphyroblasts are also wrapped by the foliated matrix and contain inclusion trails of a similar fine grain size and orientation to those in the cordierite (Fig. 7c), suggestive of broadly coeval growth prior to the development of
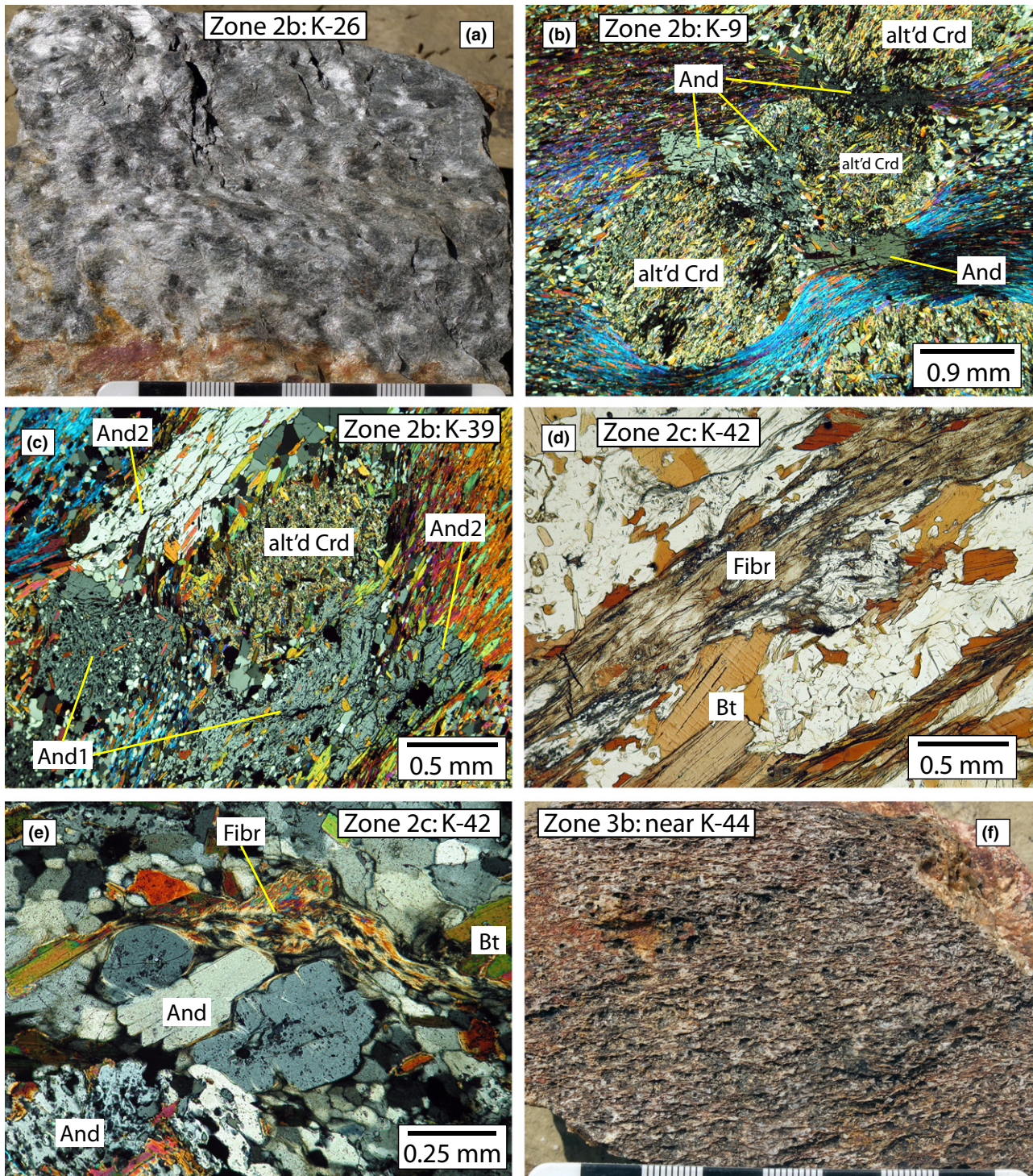
Fig. 7. Photographs and photomicrographs of schists from Kickoff Meadows area. Sample locations shown in Fig. 6. Width of major divisions on scale bar: 1 cm. (a) Photograph of typical And + Crd-bearing porphyroblastic schist from Zones 2a and 2b, with schistose fabric undulating around porphyroblasts. (b) Photomicrograph of schist from Zone 2b showing cordierite (altered) wrapped by foliated micaceous matrix, with the matrix in turn overgrown by andalusite. Andalusite has partially replaced cordierite, as revealed by the inclusion-rich andalusite on the margins of the cordierite porphyroblasts. (c) Photomicrograph of schist from Zone 2c showing two generations of andalusite: the earlier generation is filled with fine-grained inclusions similar to cordierite, whereas the later generation of andalusite has fewer, coarser inclusions and overgrows the foliated matrix fabric that wraps the cordierite and earlier generation of andalusite. (d) Photomicrograph of fibrolite-rich seam in schist from Zone 2c. (e) Photomicrograph of andalusite partly replaced by fibrolite at grain edges and along cracks. (f) Photomicrograph of foliated, fibrolite-rich hornfels from Zone 3b, with fibrolite concentrated in milky seams between pitted domains, the pits being the sites of altered cordierite porphyroblasts.

the foliated matrix fabric. More commonly, however, andalusite shows a number of textures indicative of growth later than cordierite, including: interstitial andalusite between cordierite porphyroblasts (Fig. 7b); andalusite grains that have grown across the foliated matrix fabric that wraps the cordierite porphyroblasts (Fig. 7b,c); and partial replacement of cordierite by andalusite (Fig. 7b; and fig. 15c of Pattison et al., 2011).

Zone 2b: Sparse fibrolite zone (730–220 m)

Zone 2b is substantially wider than at Cobalt Lake (510 m v. 40 m). Rocks from this zone look the same as those in Zone 2a, and contain the same mineral assemblage and textures, with the exception of the presence of modally minor ($\ll$0.1 vol.%) acicular crystals and aggregates of fibrolite only visible in thin section. The amount of fibrolite increases gradually going upgrade in this zone (unquantified observation), but it is sporadically distributed in the rocks, sometimes weakly associated with biotite grains or quartz segregations.

Zone 2c: Sillimanite zone (220–100 m) – western area only

Zone 2c is restricted to the western portion of the Kickoff Meadows area, and occupies a zone ~120 m wide (Fig. 6). It is characterized by an increase in the abundance of fibrolitic sillimanite, locally exceeding ~1 vol.% (modal estimation is difficult because of its fibrous nature). In contrast, in the eastern part of the Kickoff Meadows area, Zone 2b (minor fibrolite) continues up until Zone 3a.

The fibrolite in Zone 2c occurs in isolated aggregates and discrete, elongate, swirly masses and seams, commonly in association with biotite, andalusite and sometimes tourmaline (Fig. 7d,e). In hand sample these are visible in the form of fibrous white knots and stringers with a silky appearance, typically aligned with the schistosity (Fig. 7f). In many rocks from this zone, fibrolite has partially replaced biotite or andalusite, the latter along cracks and grain boundaries (Fig. 7e). These features are irregularly distributed in the rocks: on a scale of less than a few millimetres, there can be relatively fresh grains of andalusite and biotite adjacent to grains that have been largely replaced. Together, these characteristics suggest that fibrolite development is due at least in part to a locally catalysed, most likely fluid-fluxed, process.

Apart from a few rocks at the lower grade end of the zone, most rocks in Zone 2c lack primary, schistosity-defining muscovite (coarse retrograde muscovite, as described at Cobalt Lake, is variably present in many samples). The rocks consequently are darker in colour than the schists in Zone 2b. Porphyroblasts of andalusite and cordierite are still present, but the cordierite commonly appears corroded compared to lower grades.

Zone 3a: Muscovite + K-feldspar zone (120–80 m) – eastern area only

Zone 3, defined by the presence of metamorphic K-feldspar, is narrower at Kickoff Meadows than at Cobalt Lake (120 m v. 260 m). Zone 3a, characterized by the coexistence of primary muscovite and K-feldspar, occurs only in the eastern traverse of Kickoff Meadows over an interval of ~40 m. K-feldspar is present in minor amounts and typically has a microperthitic texture, like at Cobalt Lake. The rocks contain conspicuous fibrolitic sillimanite. In contrast to Cobalt Lake, there is no evidence for a new generation of andalusite in the K-feldspar-bearing samples.

Zone 3b: K-feldspar zone (100–0 m)

Zone 3b is characterized by the absence of primary muscovite and sporadic presence of K-feldspar. In the western area, the low-grade boundary of this zone is marked by the appearance of K-feldspar, whereas in the eastern area, it is marked by the disappearance of primary muscovite (Fig. 6).

The rocks in Zone 3b are generally foliated but more granoblastic than at lower grades. The abundance of K-feldspar is greater in the eastern domain than in the western domain, mirroring the relative abundance of muscovite at lower grades in the two areas. The location of the K-feldspar-in isograd in the western area is likely masked by the absence of the appropriate muscovite-bearing protoliths. In the eastern area, the loss of primary muscovite is accompanied by an increase in the abundance of sillimanite and K-feldspar.

Zone 3c: Migmatite zone

A number of outcrops within ~50 m of the intrusive contact are migmatitic, as revealed by more ductile fabrics and mm–cm-scale segregations and veins of quartzofeldspathic material (DeBuhr, 1999). The segregations in the eastern area are typically rich in K-feldspar, plagioclase and quartz, whereas they may be free of K-feldspar in the western area.

Iceberg Lake and Bugaboo Glacier areas

The Iceberg Lake and Bugaboo Glacier areas were examined in less detail than the Cobalt Lake and Kickoff Meadows area. Like Kickoff Meadows, the two areas are dominated by schists. Figures S6 and S7 show metamorphic maps of the Iceberg Lake and Bugaboo Glacier areas, respectively, and Table S1 gives types and numbers of mineral assemblages as a function of distance from the contact (21 and 13 samples examined, respectively).

In the Iceberg Lake area, the intrusive contrast dips relatively shallowly outwards (50°) beneath the host metasedimentary rocks like at Cobalt Lake.

Modal changes with grade - Cobalt Lake Transect
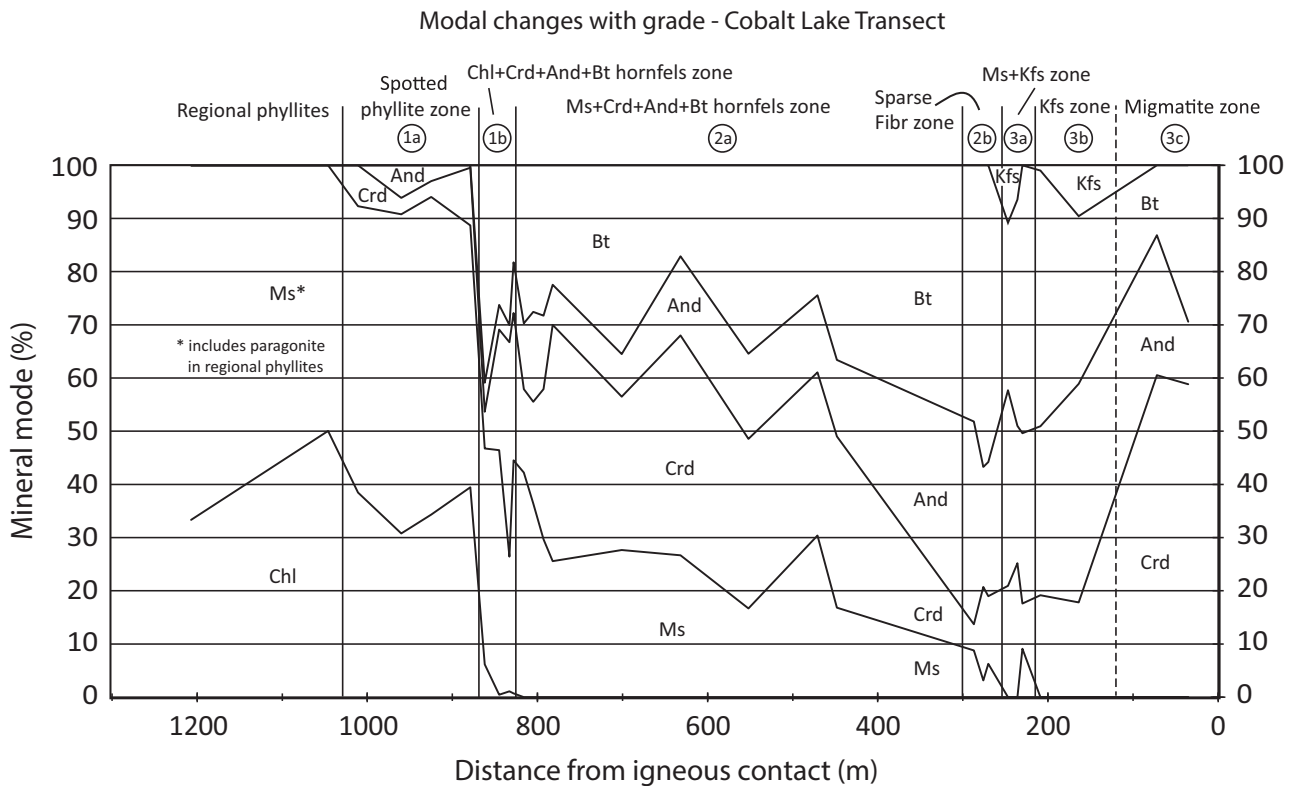
Fig. 8. Graph of modal mineralogy as a function of distance from intrusive contact at Cobalt Lake. Raw data in Table S2. The modes of quartz and plagioclase have been omitted and the remaining mineralogy re-normalized to 100% (see text).

Several samples from Zones 2a and 2b preserve textural evidence for two generations of andalusite (Fig. S8b,c). In Fig. S8c, and in a magnified view of the same texture in fig. 5f of Pattison *et al.* (2002), intergrown andalusite and biotite occur in bands between, and in places replacing, cordierite.

Henrichsen (2000) examined the aureole between Cobalt Lake and Bugaboo Glacier (Fig. 1), focusing on the transition from hornfels-dominated textures in the Cobalt Lake area to schistose textures in the vicinity of Bugaboo Glacier (Fig. S7). The transition occurs over a relatively narrow interval, approximately coinciding with a transition from mixed pelite/psammite (Cobalt Lake area) to more psammite-dominated lithologies in the inner part of the aureole (Bugaboo Glacier area). Zone 2 at Bugaboo Glacier contains the coarsest grained porphyroblastic schists in the aureole (Fig. S8d,e). Locally andalusite + tourmaline-bearing quartz veins occur in quartzose layers interbedded with the schists (Fig. S8f).

MODAL VARIATIONS

Variations in modal mineralogy in the Cobalt Lake transect as a function of grade are shown in Fig. 8, based on analysis of 33 samples labelled in Fig. 2 and listed in Table S2. Modes for 24 of the samples

were obtained in a three-stage process: (i) optical point counting, in which, for low-grade samples with a fine-grained matrix, the matrix was treated as one phase; (ii) for the samples with a fine-grained matrix, point counting of back-scattered electron (BSE) images of five representative areas of the matrix; and (iii) integration of the two data sets. Six additional low-grade samples were analysed by area estimation of BSE images, and three additional high-grade samples, all altered, were estimated optically by eye. In Fig. 8, the modes of quartz and plagioclase are omitted because their abundance reflects mainly sedimentary processes; the remaining minerals are re-normalized to 100%.

The jagged trends in Fig. 8 reflect control by both bulk composition and metamorphic grade. A few grade-related trends emerge that are consistent with the textural observations: modally minor development of cordierite and/or andalusite, in the absence of biotite, in the spotted phyllite zone (Zone 1a); an abrupt decrease in chlorite and increase in cordierite, andalusite and biotite going through narrow Zone 1b; a gradual decrease in muscovite and cordierite and increase in andalusite and biotite going through Zones 2a and 2b, a trend that is mirrored in variation of Crd/(Crd + And) with grade (Fig. 9a); and loss of muscovite and development of K-feldspar over a narrow zone of co-existence in Zone 3a.
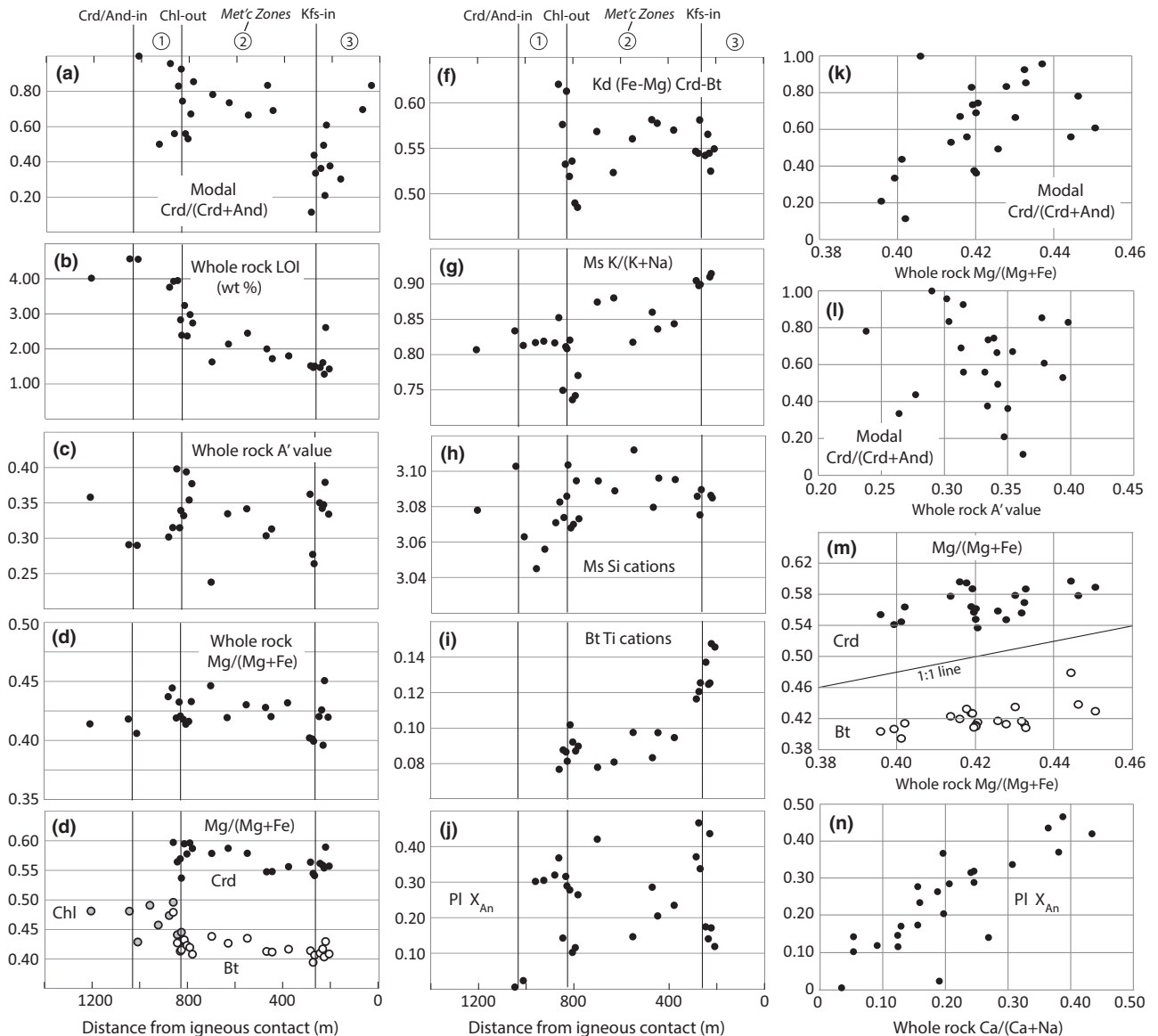
Fig. 9. (a–j) Variations in modal mineralogy, bulk rock chemical parameters and mineral chemical parameters *v.* distance from the igneous contact in the Cobalt Lake area. (k–n) Cross plots of modal ratios, and selected mineral chemical parameters, *v.* bulk rock chemical parameters. In (m), the '1:1' line is the line along which an increase in Mg/(Mg + Fe) of 0.01 in the whole rock is matched by an increase in Mg/(Mg + Fe) of 0.01 in cordierite or biotite. Raw data for plots in Tables S3 and S4–S12.

WHOLE-ROCK AND MINERAL CHEMICAL VARIATIONS

The average and range of whole-rock compositions from the Cobalt Lake area are plotted in an AFM diagram in Fig. 10a, and trends in mineral-compositional parameters as a function of grade are shown in Fig. 9. The data come from Tables S3–S12. Analytical procedures are described in DeBuhr (1999). Carbon and sulphur were not analysed because the rocks are non-graphitic and contain little sulphide.

Whole-rock loss on ignition, primarily dependent on whole-rock water content, decreases markedly with the consumption of chlorite, and continues to decrease gradually as grade increases (Fig. 9b). Whole-rock compositions plot in a tight cluster in the AFM diagram Fig. 10a. Variations in Si, Na and Ca (Table S4) are accounted for in Fig. 10a by projection from quartz and feldspar. The mean and range of aluminium index [$A' = (Al–3K–Na−2\,Ca)/2$] is 0.34 (0.24–0.44), and of Mg/(Mg + Fe) is 0.42 (0.40–0.45; Table S3); when projected from ilmenite, the average whole-rock Mg/(Mg + Fe) increases to 0.45 (Fig. 10a; Table S3). The A' value is typical of aluminous pelites (Spear, 1993), those that plot above the garnet–chlorite tie-line in the AFM diagram
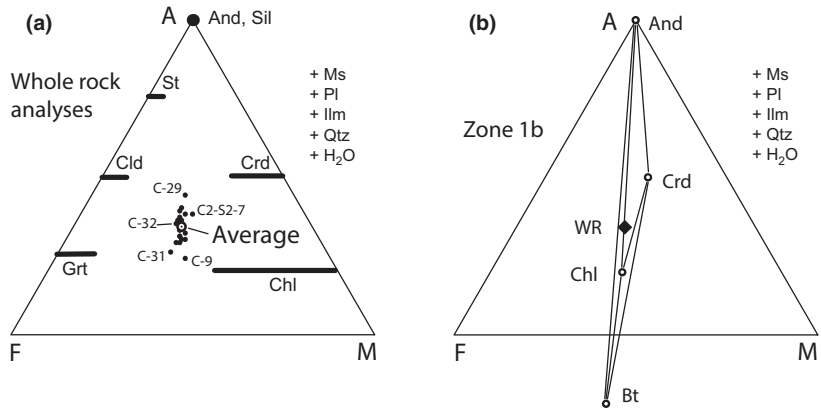
Fig. 10. (a) AFM diagram showing plotting positions of rock compositions from the Cobalt lake area. Raw data in Tables S3 and S4. (b) AFM diagram showing plotting positions of average cordierite, biotite, chlorite and whole rock compositions of the four samples from Zone 1b of the aureole. Raw data in Tables S3, S4, S5, S7 and S9.

(Fig. 10a). Whole-rock A' and Mg/(Mg + Fe) show some scatter within individual metamorphic zones but no significant variation with grade (Fig. 9c,d). There is a weak correlation between modal Crd/(Crd + And) and whole-rock Mg/(Mg + Fe) (Fig. 9k), but none between modal Crd/(Crd + And) and whole-rock A' value (Fig. 9l).

Cordierite and biotite are unzoned compositionally. The Mg/(Mg + Fe) of cordierite, biotite and chlorite co-vary with one another and show little variation with grade, possibly a weak trend to more Fe-rich compositions; they average 0.57, 0.42 and 0.46 respectively (Fig. 9e; and fig. 8 of Pattison et al., 2002). The Kd (Fe–Mg) between cordierite and biotite shows no significant variation with grade, similar to the Ballachulish aureole (Pattison & Harte, 1991), averaging 0.55 (Fig. 9f). The only significant correlation of Mg/(Mg + Fe) in cordierite and biotite, apart from each other, is with whole-rock Mg/(Mg + Fe) (Fig. 9m; and fig. 14b of Pattison et al., 2011).

The K/(K + Na) in muscovite increases with grade from ~0.8 outside the aureole to ~0.9 in Zone 3a (Fig. 9g), apart from a small population of samples with Na-richer muscovite in the vicinity of the Zone 1b/Zone 2a boundary. Outside the aureole, paragonite-rich white mica coexists with muscovite (Fig. 3b), but obtaining reliable analyses of paragonite is difficult because of the fine grain size; the measured range of K/(K + Na) in three samples is 0.27–0.59 (Tables S3 & S6), with the lowest value probably being the most accurate (least chance of being a mixed analysis). Jamieson et al. (2012) reported K/(K + Na) values of white mica from argillaceous host rocks to the Halifax Pluton, whose aureole bears a number of similarities to the Bugaboo aureole, to be in the range 0.5–0.7. Tschermak content of muscovite, as measured by Si cations per 11-oxygen formula unit, averages 3.08 and shows no significant variation with grade, apart from some lower values in Zone 1a (Fig. 9h). The Ti content of biotite increases in the vicinity of the Zone 2/3 boundary from 0.08 to 0.10 cations per 11-oxygen formula unit to 0.12–0.15 cations (Fig. 9i).

Plagioclase compositions (X_{An}) vary significantly within individual samples (Tables S3 & S10). Mean values for individual samples also vary widely, ranging in X_{An} from 0.01 to 0.58, with no consistent variation with grade apart from albitic compositions in two low-grade samples (Fig. 9j). The strongest correlation of mean X_{An} in plagioclase is with whole-rock Ca/(Na + Ca) (Fig. 9n). Plagioclase in a few samples spans the compositional range of the peristerite gap (Table S3), but clear evidence of a compositional gap was not found.

PROGRADE REACTIONS IN THE BUGABOO AUREOLE INFERRED FROM PETROGRAPHY

In this section, prograde reactions in the aureole are inferred from the modal and textural changes described above. These involve a relatively small number of minerals whose compositions are largely represented in the KFMASH chemical system (K_2O–FeO–MgO–Al_2O_3–SiO_2–H_2O). Exceptions are the biotite-free mineral assemblages in Zone 1a interpreted to have formed from the reaction of paragonite-rich white mica, suggesting reactions dominantly in the NFASH/NMASH chemical system (Na_2O–FeO/MgO–Al_2O_3–SiO_2–H_2O).

Zone 1a: Spotted phyllite zone

The loss of paragonite-rich white mica from the regional phyllites, concomitant with the development of neoblasts of andalusite, cordierite and plagioclase, without biotite, suggests reactions of the form:

$$Pg + Qtz \rightarrow And + Ab + H_2O \qquad (1)$$

$$Pg + Chl + Qtz \rightarrow Crd + Ab + H_2O \qquad (2)$$
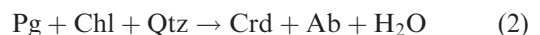
Figure 11a shows a schematic Schreinemakers' analysis involving these reactions in either the NFASH or NMASH system; expansion of the system to NFMASH or KNFMASH changes the univariant
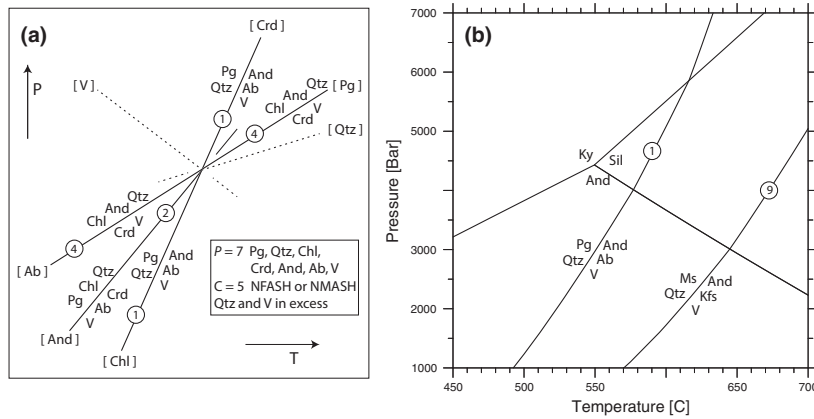
Fig. 11. (a) Schematic Schreinemakers' grid of biotite-free reactions involving paragonite, chlorite, cordierite and andalusite in the simplified NFASH (or NMASH) chemical system. (b) *P–T* diagram, calculated with the HP data set, showing the *P–T* position of end-member reactions 1 and 9.

reactions in Fig. 11a into multivariant bands. The restriction of plagioclase porphyroblasts to andalusite-bearing assemblages suggests at least the operation of reaction 1. The potassium component of the paragonite-rich white mica that was consumed in this reaction most likely entered the abundant muscovite-rich white mica in the rocks.

The source of Ca in the regional phyllites needed to produce the anorthite component in the plagioclase porphyroblasts is uncertain. Carbonate minerals are not observed in the regional phyllites and, in the few regional phyllites that contain plagioclase, the plagioclase is albitic (Table S3). In plagioclase-free, paragonite-bearing regional phyllites, margarite-rich mica has not been observed, and the margarite component in the paragonite and muscovite is negligible (Table S6). A possible source of Ca in the regional phyllites is apatite, although a quantitative analysis of complementary phosphate phases in the porphyroblastic rocks, needed to balance the possible transfer of Ca from apatite to plagioclase, has not been performed.

In the cordierite-bearing, andalusite-free samples in Zone 1a, the lack of evidence for plagioclase growth accompanying cordierite growth makes the operation of reaction 2 uncertain. Another possible mechanism to produce cordierite in the absence of biotite involves compositional change in the modally abundant muscovite and chlorite via the Tschermak (Tsch) exchange $[(Fe,Mg)_{-1}Si_{-1} = Al_2]$, as discussed in Pattison (1987, pp. 266–271). In the reaction:

$$Chl + Qtz + Tsch \rightarrow Crd + H_2O \qquad (3)$$
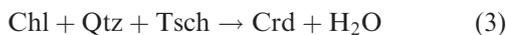
chlorite and muscovite become more Si-rich, releasing Al to react with chlorite and quartz to yield cordierite. Examining the measured mineral compositions in Table S3 and Fig. 9h, however, Si content of muscovite (a measure of Tschermak exchange) shows no significant variation with grade. This suggests that, if reaction 3 did occur, it could only have resulted in subtle compositional change in the sheet

silicates and modest production of cordierite. Even if thermodynamically feasible, it is further uncertain whether the energetic driving force associated with these subtle compositional changes, involving tetrahedrally coordinated Al and Si, would be sufficient to overcome the kinetic barriers to their progress at these relatively low temperatures (e.g. Dempster, 1992).

In biotite-free, And + Crd-bearing samples, the following reaction can be written:

$$And + Chl + Qtz \rightarrow Crd + H_2O. \qquad (4)$$

Reaction 4, shown in Fig. 11a, is possible if andalusite developed at low grade, such as by reaction 1, and then became a reactant in reaction 4. However, spatial and textural evidence argues against this possibility: andalusite- and cordierite-bearing assemblages are randomly distributed in Zone 1a (Fig. S2), and andalusite shows no evidence of consumption.

The few biotite-bearing samples in Zone 1a contain cordierite but no andalusite, implying operation of the model reaction (divariant in KFMASH):

$$Ms + Chl + Qtz \rightarrow Crd + Bt + H_2O. \qquad (5)$$

Zone 1b: And–Crd–Bt–Chl zone

The marked modal increase in cordierite, andalusite and biotite and modal decrease in chlorite going upgrade through Zone 1b implies operation of the model reaction (univariant in KFMASH):

$$Ms + Chl + Qtz \rightarrow And + Crd + Bt + H_2O. \qquad (6)$$

Figure 10b shows an AFM diagram on which are plotted the average biotite, cordierite, chlorite and whole-rock compositions from the four analysed samples from Zone 1b (Table S3). Chlorite plots in an interior position to the other three minerals, as found in all other localities in which these minerals co-exist (Pattison, 1987), implying a reaction relationship as written above. DeBuhr (1999) used a mass

balance approach based on singular value decomposition (Fisher, 1989) to estimate the stoichiometry of reaction 6 for the four samples from Zone 1b. A representative example is that calculated for sample C–6, normalized to 1 mol of cordierite:

$$6.0\,Ms + 3.0\,Chl + 0.4\,Qtz + 0.4\,Ilm$$
$$= 5.7\,And + 5.2\,Bt + 1.0\,Crd + 0.8\,Ab + 25.6\,H_2O.$$
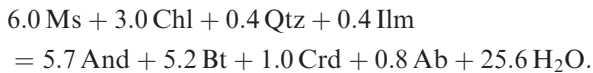
In this mass balance, muscovite and biotite are calculated for a 11-O formula unit, and chlorite for a 14-O formula unit (Tables S5, S6 & S9).

The ~50 m width of Zone 1b represents the reaction interval for reaction 6, implying some degree of multivariancy due to additional components, or kinetic control. The two generations of inclusion-rich andalusite in some samples from Zone 1b and in the lower grade parts of Zone 2a at Cobalt Lake suggest sequential operation of reaction 1 followed by reaction 6.

In the schistose rocks from Kickoff Meadows and Iceberg Lake, microstructural evidence indicates that cordierite developed before andalusite in many samples (e.g. andalusite grows across the foliation that wraps cordierite), suggesting progress of reaction 5 prior to reaction 6. No evidence is found for the operation of paragonite-consuming reactions 1 or 2 in the Kickoff Meadows and Iceberg Lake areas, but sample coverage is sparse and mineral growth concomitant with deformation in the schists may have resulted in different and possibly less distinctive textures than in the hornfelses at Cobalt Lake.

Zone 2a: And–Crd–Bt zone

In Zone 2a, gradual modal decrease in muscovite + cordierite concomitant with increase in andalusite + biotite (Fig. 8), and microstructures indicating andalusite growth post-dating cordierite, suggest progress of the reaction (divariant in the model KFMASH system):

$$Ms + Crd \rightarrow And + Bt + Qtz + H_2O. \qquad (7)$$
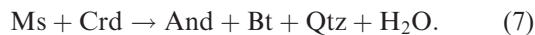
A possible caveat to the textural interpretation is kinetic control on porphyroblast development. Waters & Lovegrove (2002) provided textural evidence for the development of cordierite prior to andalusite in the Bushveld aureole, even though the chlorite-consuming, cordierite-producing reaction was predicted to be metastable relative to, and occur at a higher temperature than, the chlorite-consuming, andalusite-producing reaction. Their interpretation was that andalusite was delayed in its nucleation and growth compared to cordierite due to its higher interfacial energy. Once reaction initiated, both minerals grew from the consumption of matrix minerals, with growth of the more stable andalusite eventually superseding that of cordierite.

Such a scenario could potentially account for textures in Zone 2 of the Bugaboo aureole that simply indicate growth of andalusite later than cordierite in the Bugaboo aureole. However, it does not satisfy the other textural observations in Zone 2, such as: the evidence for matrix coarsening and porphyroblast/matrix reorientation between the initial development of cordierite ± andalusite porphyroblasts and the later development of andalusite crystals and rims, suggesting a distinct later episode of andalusite growth; and the evidence for replacement of cordierite by intergrown andalusite + biotite. Consequently, forward progress of reaction 7, as written above, is still favoured.

Despite the modal and textural evidence, there is no mineral chemical evidence for progress of reaction 7 as written, in particular anticipated Mg-enrichment of co-existing cordierite and biotite (see discussion in Pattison et al., 2002). Rather, cordierite and biotite show little variation in Mg/(Mg + Fe) with grade (Fig. 9e). One possibility is that the natural reaction is more complex than as written, involving other Fe-bearing phases like ilmenite. Another possibility is that the energetic driving force to effect the relatively small compositional changes in the minerals was too small to overcome the intracrystalline and intercrystalline kinetic barriers in the exchange process. Pattison et al. (2011) have shown that reaction 7 involves a very small free energy change. It may be that the minerals acquired their present compositions in the interval of vigorous reaction, fluid release and recrystallization accompanying chlorite consumption by reactions 5 or 6, and changed little thereafter. Finally, bulk rock variability may have influenced the observed trend in Mg/(Mg + Fe), as discussed below.

Zones 2b and 2c: Sparse fibrolite zone and Sillimanite zone

The reaction accounting for the sporadic development of sparse fibrolitic sillimanite in Zone 2b at Cobalt Lake is uncertain. There is no consistent spatial relationship between fibrolite and andalusite, or evidence of andalusite dissolution, that might be suggestive of the polymorphic reaction:

$$And \rightarrow Sil. \qquad (8)$$

Evidence for operation of reaction 8 is, however, seen in higher grade samples (e.g. Fig. 7e). Possibilities for the incipient development of fibrolite include a local fluid-catalysed reaction (e.g. Vernon, 1979), or progress of reaction 7 in the sillimanite rather than andalusite stability field.

In the Kickoff Meadows area, evidence in support of sillimanite production by reaction 7 is found in the transition between Zones 2b and 2c, where fibrolite increases in modal abundance in the same interval in which primary muscovite becomes sparse or absent. Widespread evidence for fluid control on the

development of sillimanite is found in Zones 2b and 2c of the Kickoff Meadows, Iceberg Lake and Bugaboo Glacier areas, in which fibrolitic sillimanite is locally developed in discrete seams and segregations parallel to the foliation, sometimes associated with tourmaline, whereas interfolial parts of the rock are free of sillimanite.

Zone 3a: Muscovite–K-feldspar zone

In Zone 3a in the Cobalt lake area, the development of K-feldspar porphyroblasts and a new generation of andalusite, concomitant with the loss of muscovite across this zone, implies progress of the muscovite breakdown reaction:

$$Ms + Qtz \rightarrow And + Kfs + H_2O. \qquad (9)$$

A complication in this interpretation at Cobalt Lake is the sporadic occurrence of sparse sillimanite at lower grade in Zone 2b, from which one would anticipate that sillimanite rather than andalusite would be produced at higher grade by reaction 9. Although fibrolitic sillimanite is present in the Kfs-bearing rocks, it is only in minor modal abundance. These observations are interpreted to indicate a pressure of metamorphism at Cobalt Lake close to the intersection of reactions 8 and 9.

In Zone 3a in the eastern part of the Kickoff Meadows area, K-feldspar development is not accompanied by an obvious new generation of andalusite, and sillimanite is more abundant than in Zone 3a at Cobalt Lake. These features suggest that reaction 9 produced sillimanite rather than andalusite in this locality.

Zone 3b: K-feldspar zone

There are no distinctive features of this zone implying reaction. Some samples from Cobalt Lake show evidence for recrystallization of cordierite. Based on two samples, there is an apparent increase in the cordierite:andalusite modal ratio in this zone at Cobalt Lake (Fig. 8), but neither of these rocks is migmatitic or contains K-feldspar that would be suggestive of progress of the reaction:

$$Bt + And/Sil + Qtz \rightarrow Crd + Kfs + H_2O \text{ or } L \text{ (melt)}. \quad (10)$$

Zone 3c: Migmatite zone

Migmatites are sporadically developed in the highest grade part of Zone 3 in the aureole. The intermingling of migmatitic and non-migmatitic rocks, the lack of difference in mineral assemblage between the two, and the absence of K-feldspar in many of the rocks, argues against dehydration melting reactions involving biotite. Muscovite is consumed downgrade

of the migmatitic rocks and so could not have been involved.

The most likely melting reaction is therefore a locally fluid-fluxed melting reaction involving mainly feldspar and quartz, such as:

$$Pl \pm Kfs + Qtz + H_2O \rightarrow L(melt). \qquad (11)$$
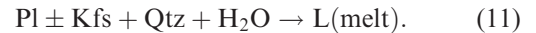
A possible source of the introduced fluid is the crystallizing intrusion, as suggested by the local occurrence of migmatites on Northpost Spire to the north of Cobalt Lake, vertically above the igneous contact that dips outward beneath the locally migmatized rocks; fluids escaping upwards from the crystallizing intrusion may have locally fluxed melting in the overlying metasedimentary rocks (cf. Pattison & Harte, 1988). In the Kickoff Meadows area, where the metasedimentary rocks dip steeply beneath the intrusion, fluids released from metapelitic dehydration reactions may have contributed to the migmatization (cf. Johnson et al., 2003).

Synthesis of reactions inferred from petrography

The inferred reactions and metamorphic zones from Cobalt Lake and Kickoff Meadows are synthesized in a schematic phase diagram in Fig. 12. The qualitative topology of the phase diagram matches that of earlier studies of low-P contact metamorphism of pelites (e.g. fig. 36 of Pattison & Tracy, 1991; fig. 8 of Pattison & Vogl, 2005). Most of the reactions in Fig. 12 are divariant or univariant reactions in KFMASH, with the exception of low-grade reactions in Zone 1a that involve paragonite, and the melting reaction in Zone 3c that involves plagioclase. Additional chemical components in the natural rocks render the KFMASH reactions multivariant, although it is unlikely that they will have significantly modified the dominant modal and textural changes implied by the KFMASH reactions.
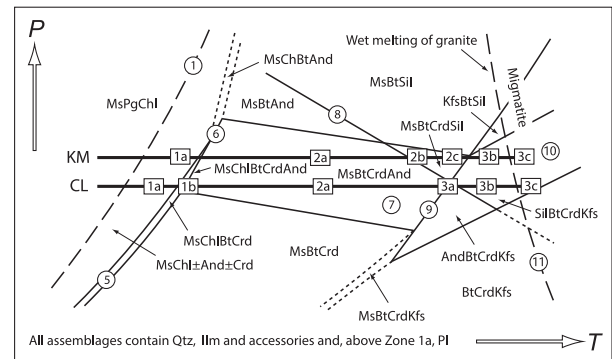
Fig. 12. Schematic phase diagram for the Bugaboo aureole synthesizing the reactions and mineral assemblage zones interpreted from modal and textural features in the aureole. The relative position of the wet melting curve is based on Fig. 13. CL, Cobalt Lake area; KM, Kickoff Meadows area.

Figure 12 was constructed assuming that the metamorphic field gradient in the aureole, as well as P–T–t path for individual samples, was sensibly isobaric. Evidence in support of this assumption includes: the steep or outwardly dipping intrusive contacts; the sharp and cross-cutting nature of the contact with respect to the host metasedimentary rocks; the continuity and coherence of structural features in the Cobalt Lake and Kickoff Meadows areas (Figs S1, S3 & S4); and the hornfelsic textures in the Cobalt Lake area, suggesting a predominantly static, thermal overprint. In the Kickoff Meadows, Iceberg Lake and Bugaboo Glacier areas, schistose textures and the reorientation of regional structures towards parallelism with the intrusive contacts imply greater degrees of deviatoric stress related to emplacement of the intrusion. However, Brace *et al.* (1970), Rutter (1976), Carmichael (1978) and Shimizu (1995) have shown that deviatoric stress is unlikely to exceed ~100 bar and can thus be largely ignored, especially in rocks undergoing devolatilization and recrystallization.

Differences in zonal sequences in the aureole in relation to pressure of contact metamorphism

Differences in the zonal sequence in the Kickoff Meadows area compared to the Cobalt Lake area suggest that the Kickoff Meadows area was metamorphosed at a greater depth (Fig. 12). These differences include: a wider Zone 2b; higher modal abundance of sillimanite in Zones 2b and 2c; loss of muscovite in most rocks in Zone 2c of the western part of the Kickoff Meadows area; and, where K-feldspar is developed in the eastern part of the Kickoff Meadows area, no evidence for accompanying growth of andalusite. Within the Kickoff Meadows area itself, some features of the eastern part are suggestive of a slightly shallower level of contact metamorphism than the western part, such as a narrower Zone 2b, lack of Zone 2c and presence of Zone 3a (Fig. 6).

These differences mean that the Bugaboo aureole straddles two of the low-P metapelitic facies series of Pattison & Tracy (1991) – Facies Series 1c (lower pressure) for the Cobalt Lake area, and Facies Series 2a (higher pressure) for the Kickoff Meadows area. The key differences between the two facies series are whether muscovite + quartz reacts out by reaction 9 to make andalusite + K-feldspar (Facies Series 1c; Cobalt Lake) or sillimanite + K-feldspar (Facies Series 2a; Kickoff Meadows), and whether sillimanite first occurs upgrade of the development of K-feldspar (Facies Series 1c) or downgrade (Facies Series 2a; Kickoff Meadows). These differences involve non-ferromagnesian minerals and so are relatively insensitive to variations in bulk composition. As noted above, a complication concerning the latter criterion at Cobalt Lake is the sporadic, modally minor fibrolite seen in some rocks downgrade of where muscovite + quartz react out in favour of andalusite + K-feldspar.

COMPARISON OF PHASE DIAGRAM PREDICTIONS WITH NATURAL OBSERVATIONS

In this section, predictions of thermodynamically calculated phase diagrams are compared with the natural observations and interpretations summarized in Fig. 12.

Thermodynamic modelling

The bulk composition of pelites in the aureole varies over a small range and shows no consistent trend with grade (Figs 9c,d & 10a). Phase diagrams were therefore calculated for the average whole-rock composition in the aureole; the composition is provided in Table S13 and in the caption to Fig. 13. Phase diagrams for five 'extreme' individual bulk compositions were also calculated to test the generality of the results obtained for the average bulk composition; the compositions are labelled in Fig. 10a and tabulated in Table S13.

The phase diagrams were calculated using the Theriak/Domino phase equilibrium modelling software (de Capitani & Brown, 1987; de Capitani & Petrakakis, 2010). Two chemical systems were investigated, MnNCKFMASHT (MnO–Na$_2$O–CaO–K$_2$O–FeO–MgO–Al$_2$O$_3$–SiO$_2$–H$_2$O–TiO$_2$) and KFMASH (system reduced from MnNCKFMASHT by projection from ilmenite, albite and anorthite and omission of MnO). Most rocks in the aureole contain ilmenite and lack magnetite, suggestive of not strongly varying, and relatively low, amounts of Fe^{3+} (Connolly & Cesare, 1993). Nevertheless, the effects of varying Fe^{3+} were investigated. In the absence of graphite, a_{H_2O} was assumed to be unity. Eighty moles of hydrogen (equivalent to 40 mol H$_2$O) was added to the anhydrous bulk composition to ensure that a_{H_2O} was unity across the phase diagram (equivalent to aqueous fluid being available as a possible reactant or product across the diagram). The compositional input file for Theriak/Domino that was used to calculate the phase diagrams in this paper is provided in Appendix S1.

Two thermodynamic databases were used. The first is that of Holland & Powell (1998), updated to version ds5.5 (hereafter referred to as the 'HP data set'). Two sets of activity–composition (a–x) relations were used with the HP data set. The first set (hereafter referred to as 'HP1') comprises the following: garnet and chlorite, Tinkham *et al.* (2001); biotite, White *et al.* (2005); plagioclase, Holland & Powell (2003; ternary feldspar, Cbar1 field); white mica, Coggon & Holland (2002; margarite component omitted); ilmenite, Tinkham & Ghent (2005; ideal ternary); melt, White *et al.* (2007); all

Fig. 13. Thermodynamically calculated phase diagrams for the average composition of metapelite in the aureole (see text for discussion). For (a, d) calculated in the KFMASH system, the bulk composition in moles is: Si 79.10; Al 41.99; Fe^{2+} 9.28; Mg 7.61; K 8.19. For (b, c), calculated in the MnNCKFMASHT system, the bulk composition in moles is: Si 92.17; Ti 1.15; Al 47.57; Fe^{2+} 10.43; Mg 7.61; Mn 0.13; Ca 0.92; Na 3.74; K 8.19. In all phase diagrams, the solid lines involve changes in AFM phases. In (b, c), dotted lines involve changes in oxide phases, and long dashed lines involve changes in white mica and feldspar. The heavier dotted line on all diagrams is the position of end-member reaction 1 from Fig. 11b. The bold, straight solid lines are metamorphic field gradients for the Cobalt Lake (CL) area that satisfy as closely as possible the observed mineral assemblage sequence. The bold, straight dashed line in (d) labelled 'KM' is the interpreted metamorphic field gradient for the Kickoff Meadows area (see text for discussion).

other phases including H$_2$O, Holland & Powell (1998). The second set (hereafter referred to as 'HP2') is essentially the recommended set of activity models in THERMOCALC version tc331, and is the same as HP1 except for: white mica, Coggon &

Holland (2002; margarite and pyrophyllite components omitted); biotite, White *et al.* (2007); garnet, White *et al.* (2007; tc331 'preferred' model); ilmenite, White *et al.* (2005). The one difference from tc331 is that Mn end-members for biotite and

garnet, assumed to mix ideally, were incorporated in the HP2 *a–x* models. Where compared, Theriak/Domino reproduces the phase boundaries using THERMOCALC to within 1–2 °C.

The second thermodynamic data set is a modification of the Spear & Cheney (1989) data set, based on the Berman (1988) database with adjustments to cordierite described in the appendix to Pattison *et al.* (2002). In this paper, this data set has been further modified by decreasing the enthalpy of staurolite by 3000 J so as to allow a St + And stability field for pelites of the most typical range of Mg/(Mg + Fe) = 0.4–0.5, as indicated by numerous metapelitic prograde sequences (e.g. fig. 36 of Pattison & Tracy, 1991; fig. 8 of Pattison & Vogl, 2005). The modified data set is referred hereafter as the 'SPaC14 data set'. In the SPaC14 data set, solid solution phases are represented by a smaller number of end-members than in the HP data set, and ideal on-site mixing is assumed for all phases. The end-member and *a–x* data for SPaC14 are those listed in appendix A of Spear & Pyle (2010), except for the enthalpies of the Fe- and Mn-chlorite end-members, which are as in Pattison *et al.* (2002). The thermodynamic data files for Theriak/Domino that were used to calculate the phase diagrams in this paper are provided in Appendices S2 (HP1 and HP2) and S3 (SPaC14).

Figure 13 summarizes the results of the modelling. Figure 13a,b shows phase diagrams calculated in the KFMASH and MnNCKFMASHT systems, respectively, using the HP1 data set; Fig. 13c shows a phase diagram calculated in the MnNCKFMASHT system using the HP2 data set; and Fig. 13d shows a phase diagram calculated in the KFMASH system using the SPaC14 data set. The choice of the KFMASH chemical system for Fig. 13d was made because of the relatively simple thermodynamic expressions for solid solution phases in the SPaC14 database; a phase diagram calculated in MnNCKFMASHT using SPaC14 is insignificantly different from that calculated in KFMASH, apart from the presence of a garnet stability field above ~5 kbar. Numbered reactions in the text are labelled on the phase diagrams. The calculated position of the wet melting reaction from Fig. 13c (similar to Fig. 13b) was placed on the KFMASH phase diagrams in Fig. 13a,d for reference, recognizing that the melting reaction involves phases (plagioclase, haplogranite melt) and components (Ca and Na) that are not modelled in the KFMASH system.

Paragonite-consuming reaction 1

Figure 11b shows the calculated position of the end-member paragonite + quartz and muscovite + quartz breakdown reactions 1 and 9, based on the HP data set. The >27% muscovite component in the paragonite in the regional grade phyl-lites, and the 25–35% anorthite component of the plagioclase porphyroblasts in Zone 1a, imply that reaction 1 is more complex than as written in the end-member NASH system. However, the position of reaction 1 for the natural mineral compositions is not displaced very much in *P–T* space relative to the end-member reaction in Fig. 11b because the reduced activities of the paragonite and albite end-members in the natural minerals are about the same and thus cancel. Reaction 1 is placed as a dotted line for reference on the phase diagrams in Fig. 13, recognizing that in the two Na-free KFMASH diagrams (Fig. 13a,d), it will not be stable.

In the MnNCKFMASHT phase diagram in Fig. 13b (HP1), paragonite-rich white mica is not predicted to co-exist with a muscovite-rich white mica phase anywhere on the diagram. For the likely *P–T* range of rocks at the outer edge of Zone 1a, ~2–4 kbar and 500–550 °C, a single white mica phase (muscovite, *sensu lato*) with a K:Na ratio of ~60–70:40–30 is predicted instead. In Fig. 13c (HP2), the same situation pertains except for a narrow *P–T* domain centred at ~3.5 kbar and 550 °C where paragonite is predicted to be stable. In Fig. 13c, andalusite is predicted to be modally abundant down-temperature of this domain, and to increase modestly in modal abundance along an isobaric up-temperature passage that enters and exits the paragonite-bearing domain.

These predictions contrast with the observations, namely the occurrence of two discrete white mica types in the regional phyllites downgrade of Zone 1a, the relatively K-rich composition of the muscovite co-existing with the paragonite-rich mica (K:Na ratio of ~80:20; Tables S3 & S6), and the abrupt development of andalusite and plagioclase porphyroblasts concomitant with the demise of paragonite. Three possibilities are (i) the HP thermodynamic data and/or *a–x* relations for white mica may need to be re-considered; (ii) the modelled bulk composition is not reflective of the compositions of the rocks in Zone 1a; or (iii) the discrete paragonite-rich and muscovite-rich phases in the rocks are relicts from earlier, possibly higher pressure regional metamorphism, with the micas having failed to equilibrate at the lower pressures of contact metamorphism before being involved in reaction 1.

Reaction 7: Ms + Crd = And + Bt + Qtz + H$_2$O

The main topological difference between the phase diagrams in Fig. 13, of particular relevance to the Bugaboo aureole, concerns the slope and position of chlorite-free reaction 7. These vary substantially according to chemical system, database and *a–x* relations, reflecting the small free energy difference between products and reactants of this reaction. The topology of this reaction nevertheless strongly influ-

ences how well the phase diagrams match the natural observations.

In the phase diagram calculated in KFMASH using the HP1 data set (Fig. 13a), reaction 7 occurs in the range 1–3 kbar and has a positive slope; using HP2 (not shown), it has the same slope but occurs at lower pressure by ~0.5 kbar. In the phase diagrams calculated in MnNCKFMASHT using HP1 and HP2 (Fig. 13b,c respectively), the same relative relationship broadly pertains. Using HP1 or HP 2, the slope of reaction 7 in MnNCKFMASHT is consistently shallower than in KFMASH. The reactions calculated in the MnNCKFMASHT system should in principle be better models of the natural reactions because they accommodate grade-related changes in mineral composition, assuming the thermodynamic models are adequate and the energetic driving force associated with these compositional changes are sufficient to overcome the kinetic barriers to their progress. For example, the increasing mode and Ti content of biotite with grade in Zone 2 (Fig. 9i) demands that ilmenite be involved as a reactant in reaction 7, in turn releasing Fe to the other phases. This factor, and others related to changing composition of mica and feldspar, may account for the shallower predicted slope of reaction 7 in MnNCKFMASHT than KFMASH. In the phase diagram calculated using the SPaC14 database (Fig. 13d), reaction 7 has a gentle negative slope.

Metamorphic field gradients

Straight-line metamorphic field gradients for the Cobalt Lake area were placed by eye on two of the phase diagrams in Fig. 13 in an attempt to match the sequence of reactions inferred from the modal and textural changes in the aureole with those on the phase diagrams. The key constraints are: passage through reactions 5 and 6; passage through reaction 7 such that And + Bt develop at the expense of Ms + Crd; and passage close to, but just below, the intersection of reactions 8 and 9 (see above for rationale).

In Fig. 13d, calculated using SPaC14, an isobaric metamorphic field gradient at ~3.0 kbar satisfies the mineral assemblage sequence, albeit not perfectly (the metamorphic field gradient passes just below reaction 6). In Fig. 13b, calculated using HP1 in MnNCKF-MASHT, a metamorphic field gradient with a positive slope satisfies the mineral assemblage sequence. This metamorphic field gradient implies 0.5–1.0 kbar of pressure increase between reactions 6 and 9 (Fig. 13b). Reactions 6 and 9 are the bounding isograd reactions of Zone 2 of the aureole. Assuming an average rock density of 2.7 g cm^{-3}, a pressure increase of 0.5–1.0 kbar implies a depth increase of ~1.7–3.5 km across the ~0.5 km width of Zone 2a (Fig. 2a), which is unreasonable geologically. In Fig. 13a,c, no metamorphic field gradient could be found to satisfy the natural constraints.

Guiraud et al. (2001) suggested that an isobaric metamorphic field gradient might be possible even if reaction 7 had a positive slope (resulting in And + Bt + Qtz + H$_2$O = Ms + Crd). They argued that if the water contained in the negligible pore space of the rock was consumed with minimal, petrographically negligible, reaction progress, the rock could be rendered fluid-absent or deficient (cf. Carlson, 2010), thereby allowing metastable persistence of the And + Bt assemblage upgrade. An argument against this interpretation is that there is no marked increase in cordierite and decrease in andalusite once Zone 3 is entered, as would be expected once water became available through progress of the Ms + Qtz-consuming reaction, thereby allowing the metastable reaction to proceed; rather, Crd/(Crd + And) modal ratios are at a minimum at the Zone 2/3 boundary (Fig. 9a). In addition, there is the modal and textural evidence suggesting development of andalusite after, and sometimes at the expense of, cordierite in Zone 2.

Concerning mineral compositions, the observed values of Mg/(Mg + Fe) of biotite and cordierite at the boundary between Zones 2 and 3, corresponding to reaction 9, cluster ~0.41 and 0.55, respectively (Fig. 9e), yielding a Kd (Fe–Mg) between cordierite and biotite of ~0.55 (Fig. 9f). For Fig. 13d, the predicted values are 0.40 and 0.54 (Kd = 0.57), in reasonable agreement with the observations. For Fig. 13b, the predicted values are 0.40 and 0.58 (Kd = 0.48).

Other differences between phase diagrams

The observed AFM topology of minerals involved in reaction 6 implies the reaction Ms + Chl + Qtz = Crd + And + Bt + H$_2$O (see above and Fig. 10b). Whereas this topology is predicted using the SPaC14 data set, the predicted topology using the HP data sets is Ms + And + Chl + Qtz = Crd + Bt + H$_2$O, at odds with the natural data. Significant differences in predicted Ti-bearing oxides occur between the phase diagrams calculated in MnNCKFMASHT using the HP1 and HP2 data sets (cf. Fig. 13b,c); in the natural rocks, ilmenite is the only Fe/Ti-oxide phase observed in the aureole.

Effect of Fe^{3+}

To test the effects of varying Fe^{3+}/Fe^{2+}, phase diagrams for the average Bugaboo pelite composition were calculated in MnNCKFMASHT, using the HP1 and HP2 data sets, for a whole rock Fe^{3+}/(Fe^{2+} + Fe^{3+}) value of 0.05. This level of Fe^{3+} is a maximum because magnetite is predicted to be stable throughout the low-P parts of the phase diagrams pertaining to the Bugaboo assemblages, whereas magnetite is not present in the natural rocks. Reaction 7 is displaced minimally for this level of Fe^{3+} compared to the Fe^{3+}-free system (Fig. 14b).
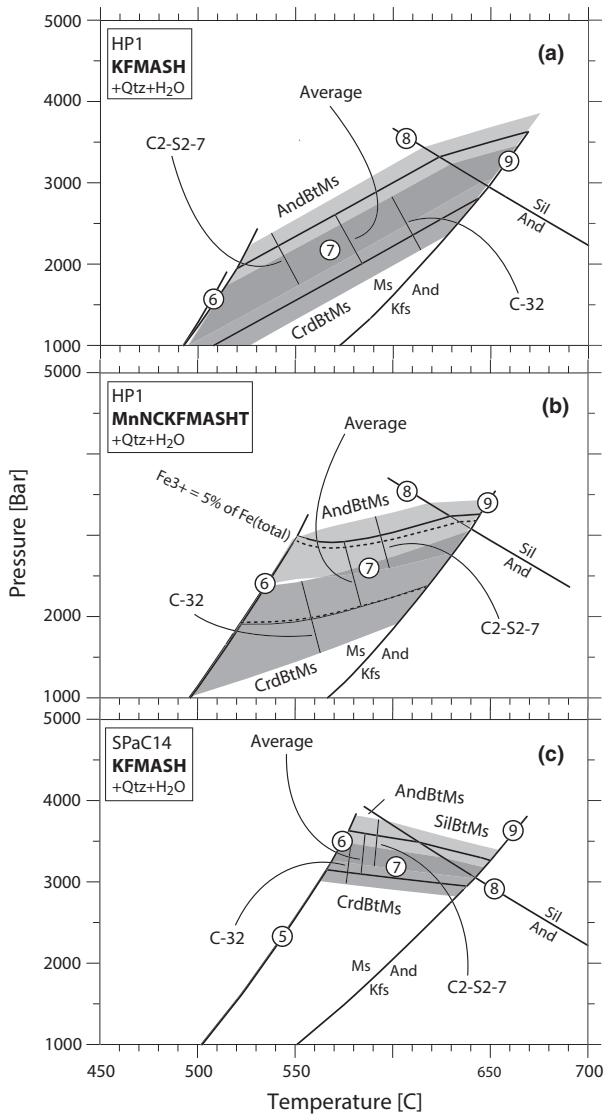
Fig. 14. Thermodynamically calculated phase diagrams for the two 'extreme' bulk compositions (samples C–32 and C2–S2–7) discussed in the text. The samples are labelled in Fig. 10a and the compositions are provided in Tables S4 and S13. The shaded bands represent the stability field for the assemblage Ms + Crd + Bt + And/Sil, which corresponds to the multivariant reaction interval for reaction 7. The solid lines are for the average Bugaboo composition and come from the respective diagrams in Fig. 13. The dotted lines show the position of the multivariant interval of reaction 7 for the average Bugaboo bulk composition in which 5% of the total iron is Fe^{3+}. The positions of reactions 5, 6, 8 and 9 for the two 'extreme' compositions are negligibly different from their position for the average composition in Fig. 13.

Effect of bulk compositional variability

To test the effect of variable bulk composition, phase diagrams like those in Fig. 13 were calculated for the five 'extreme' individual bulk compositions shown in Fig. 10a and tabulated in Table S13. The results are shown in Fig. 14, focusing on key reaction 7. The two bulk compositions showing the most extreme displacement of reaction 7 are samples C–32 and C2–S2–7; they are the most Fe-rich and Mg-rich, respectively, and are the two shown in Fig. 14. Variation in A' value mainly affects the width of the multivariant interval for reaction 7.

Compared to the position of reaction 7 for the average composition, the slopes for the extreme compositions are essentially the same and the positions are displaced by the following amounts: ±0.2 kbar for HP1 in KFMASH (Fig. 14a); ±0.5 kbar for HP1 in MnNCKFMASHT (Fig. 14b); and ±0.2 kbar for SPaC14 in KFMASH (Fig. 14c). The relative displacements using HP2 are similar to those for HP1. Although modest, these differences could account for some of the variations in mineral assemblage, mode or mineral composition in samples at approximately the same grade (Tables S1–S3; Figs 8, 9 & 11). On the other hand, these differences cannot account for the lack of anticipated Mg-enrichment in cordierite and biotite going upgrade in Zone 2, due to progress of reaction 7, because that would imply a consistent grade-related trend in whole-rock Mg/(Mg + Fe) towards Fe-rich compositions that is not seen (see Fig. 9d). In summary, bulk compositional variability blurs, but does not obscure, the petrogenetic inferences based on the average Bugaboo bulk composition.

Summary

The reasonably good agreement between the observed features in the aureole and the phase diagrams calculated with the SPaC14 database, in particular the gentle negative slope of reaction 7, is to be expected because the database was optimized to produce a negative slope for reaction 7 based on constraints from a wide range of natural settings (Pattison *et al.*, 2002). On the other hand, the more limited range of thermodynamic end-members and simpler *a–x* models, compared to the HP data sets, compromises its broader application. Concerning the HP data set and *a–x* relations, it appears that modifications may be required to model better subsolidus cordierite-bearing equilibria. Initial results from data set 6 of Holland & Powell (2011), using the *a–x* relations of White *et al.* (2014), indicate no significant change in slope or position of reaction 7 compared to HP1 or HP2 (cf. fig. 4a,b of White *et al.*, 2014).

POST-INTRUSION TILTING OF THE BATHOLITH AND AUREOLE

A deeper level of exposure of contact metamorphism is indicated at Kickoff Meadows than at Cobalt Lake (Fig. 12), based on the criteria that are independent of bulk composition (see above). Given that the present-day elevation of the two areas is similar, post-emplacement tilting of the Batholith and aureole

is implied. The maximum pressure for Kickoff Meadows, based on Fig. 13d, is ~3.5 kbar, above which staurolite rather than cordierite is predicted to form at the expense of Ms + Chl (see also Pattison & Vogl, 2005). The abundance of rocks in Zones 2a and 2b at Kickoff Meadows that contain the full mineral assemblage of reaction 7 (Ms + Crd + And ± Bt ± Sil) suggests a somewhat lower pressure than the maximum, estimated here as ~3.3 kbar (see dashed line labelled 'KM' in Fig. 13d). Compared to ~3.0 kbar for Cobalt Lake (Fig. 13), a pressure difference between the two areas of ~0.3 kbar is indicated, equating to a depth difference of ~1 km. Over a horizontal distance between the two areas of ~8 km, this depth difference implies a down-to-the-NE tilt of ~7°, within a range of 0–11° for a range of pressure difference of 0.0–0.5 kbar.

KINETIC INFLUENCES ON METAMORPHIC REACTION PROGRESS

The above interpretations focus on reactions predicted in equilibrium phase diagrams. However, a number of textural features in the aureole suggest the influence of kinetics on reaction progress.

Schists *v.* hornfelses: evidence for deformation-catalysed reaction?

The And + Crd-bearing schists in the Kickoff Meadows, Iceberg Lake and Bugaboo Glacier areas show microstructural evidence for development of cordierite prior to andalusite in most rocks, rather than approximately coeval development of the two minerals in hornfelses of the same mineral assemblage at Cobalt Lake. This observation pertains to the major development of andalusite and cordierite, due to modal consumption of chlorite, rather than to the more cryptic, less modally significant, development of the two minerals in Zone 1a at Cobalt Lake. The contrasting microtextures imply a different sequence of reactions in the schists (reaction 5, followed by reactions 6 or 7) compared to the hornfelses (reaction 6, followed by reaction 7).

In most of the schists, the period of main foliation development occurred during or following the growth of cordierite, but prior to the development of andalusite (Figs 7 & S8). Growth of cordierite via chlorite-consuming reaction 5 is expected to have resulted in a discrete, vigorous period of fluid release and rock recrystallization, which in turn would have resulted in rheological weakening of the rock. The strong schistosity now seen in the rocks developed at this time, with the most likely source of the deviatoric stress being emplacement of the intrusion. Continued heating would have resulted in subsequent growth of andalusite either by reaction 6, if any chlorite remained in the rock following growth of cordierite, or by reaction 7.

The slightly higher pressure of metamorphism of the schists compared to the hornfelses (see above) does not account for reaction 5 occurring before reaction 6 in the schists because reaction 5 is increasingly favoured (occurs at increasingly lower temperature) relative to reaction 6 as pressure decreases (Figs 12 & 13d). In addition, the contrasting microstructures are seen where the schists and hornfelses are in close proximity, such as in the region between Cobalt Lake and Bugaboo Glacier (Fig. S8). The implication is that differing degrees of deformation may have affected the kinetics of porphyroblast development. Assuming that deformation lowers rather than raises the kinetic barriers to reaction, resulting in reaction closer to equilibrium, a further implication is that there was a greater degree of thermal overstepping in the hornfelses compared to the schists before significant reaction related to chlorite breakdown initiated. Whereas reaction 5 is predicted to occur down-temperature of reaction 6, its onset in the hornfelses appears to have been delayed such that reaction 6 became the dominant chlorite-consuming reaction. The magnitude of the thermal overstep is unknown but could have been as little as a few degrees, given the small (<10 °C) separation between the predicted equilibrium positions of reactions 5 and 6 (Fig. 13d).

Decrease in grain size of porphyroblasts with grade: evidence for heating rate-controlled reaction?

At Cobalt Lake, the grain size of andalusite and cordierite porphyroblasts approximately halves between the Zone 1b/Zone 2a boundary and the middle and upper parts of Zone 2a (cf. Fig. 4a,e), even though the mineral assemblage is the same and rocks closer to the contact attained higher peak temperatures. The simplest explanation for this observation is different heating rates during development of cordierite and andalusite at the expense of chlorite via reaction 6. Zone 1b, which represents the arrested reaction interval for reaction 6, will have experienced the slowest heating rate possible for reaction 6 to proceed, and the longest time at conditions of the reaction, compared to locations closer to the contact that will have passed through the threshold temperature of the reaction more rapidly (e.g. see pp. 23–26 and fig. 12 of Pattison & Harte, 1997). The expected result is the development of a smaller number of larger crystals, as observed.

REFERENCES

Archibald, D.A., Krogh, T.E., Armstrong, R.L. & Farrar, E., 1984. Geochronology and tectonic implications of magnetism and metamorphism, Southern Kootenay Arc and neighbouring regions, southeastern British Columbia. Part II: mid-Cretaceous to Eocene. *Canadian Journal of Earth Sciences*, **21**, 567–583.

Berman, R.G., 1988. Internally-consistent thermodynamic data for minerals in the system $Na_2O–K_2O–CaO–MgO–FeO–Fe_2O_3–Al_2O_3–SiO_2–TiO_2–H_2O–CO_2$. *Journal of Petrology*, **29**, 445–522.

Brace, W.F., Ernst, W.G. & Kallberg, R.W., 1970. An experimental study of tectonic overpressure in Franciscan rocks. *Geological Society of America Bulletin*, **81**, 1325–1338.

Brandon, A.D., 1992. *Trace Element and Isotopic Constraints for the Origin of Mesozoic Granitoids in the Southern Canadian Cordillera*. Doctoral thesis, University of Alberta, Edmonton, AB, 218 pp.

de Capitani, C. & Brown, T.H., 1987. The computation of chemical equilibria in complex systems containing non-ideal solutions. *Geochimica et Cosmochimica Acta*, **51**, 2639–2652.

de Capitani, C. & Petrakakis, K., 2010. The computation of equilibrium assemblage diagrams with Theriak/Domino software. *American Mineralogist*, **95**, 1006–1016.

Carlson, W.D., 2010. Dependence of reaction kinetics on H_2O activity as inferred from rates of intergranular diffusion of aluminium. *Journal of Metamorphic Geology*, **28**, 735–752.

Carmichael, D.M., 1978. Metamorphic bathozones and bathograds: a measure of the depth of post metamorphic uplift and erosion on the regional scale. *American Journal of Science*, **278**, 769–797.

Coggon, R. & Holland, T.J.B., 2002. Mixing properties of phengitic micas and revised garnet–phengite thermobarometers. *Journal of Metamorphic Geology*, **20**, 683–696.

Connolly, J.A.D. & Cesare, B., 1993. C–O–H–S fluid compositions and oxygen fugacity in graphitic metapelites. *Journal of Metamorphic Geology*, **11**, 379–388.

DeBuhr, C.L., 1999. *Metamorphic Petrology and Mass Balance Analysis in the Bugaboo Contact Aureole*. Doctoral thesis, University of Calgary, Calgary, AB, Canada, 302 pp.

Dempster, T.J., 1992. Zoning and recrystallisation of phengitic micas: implications for metamorphic equilibration. *Contributions to Mineralogy and Petrology*, **109**, 526–537.

Fisher, G.W., 1989. Matrix analysis of metamorphic mineral assemblages and reactions. *Contributions to Mineralogy and Petrology*, **102**, 69–77.

Guiraud, M., Powell, R. & Rebay, G., 2001. H_2O in metamorphism and unexpected behavior in the preservation of metamorphic mineral assemblages. *Journal of Metamorphic Geology*, **19**, 445–454.

Henrichsen, M., 2000. *Metamorphic Petrology and Thermal Modeling in the Bugaboo Contact Aureole*. Bachelor's thesis, University of Calgary, Calgary, AB, Canada, 45 pp.

Holland, T.J.B. & Powell, R., 1998. An internally consistent thermodynamic data set for phases of petrological interest. *Journal of Metamorphic Geology*, **16**, 309–344.

Holland, T.J.B. & Powell, R., 2003. Activity–composition relations for phases in petrological calculations: an asymmetric multicomponent formulation. *Contributions to Mineralogy and Petrology*, **145**, 492–501.

Holland, T.J.B. & Powell, R., 2011. An improved and extended internally consistent thermodynamic dataset for phases of petrological interest, involving a new equation of state for solids. *Journal of Metamorphic Geology*, **29**, 333–383.

Jamieson, R.A., Hart, G.G., Chapman, G.G. & Tobey, N.W., 2012. The contact aureole of the South Mountain Batholith in Halifax, Nova Scotia: geology, mineral assemblages and isograds. *Canadian Journal of Earth Sciences*, **49**, 1280–1296.

Johnson, T.E., Gibson, R.L., Brown, M., Buick, I.S. & Cartwright, I., 2003. Partial melting of metapelitic rocks beneath the Bushveld Complex, South Africa. *Journal of Petrology*, **44**, 789–813.

Kerrick, D.M., ed., 1991. Contact metamorphism. *Mineralogical Society of America, Reviews in Mineralogy*, **26**, 847.

Kretz, R., 1983. Symbols for rock-forming minerals. *American Mineralogist*, **68**, 277–279.

Pattison, D.R.M., 1987. Variations in Mg/(Mg+Fe), F, and (Fe, Mg)Si=2Al in pelitic minerals in the Ballachulish thermal aureole, Scotland. *American Mineralogist*, **72**, 255–272.

Pattison, D.R.M., 1992. Stability of andalusite and sillimanite and the Al_2SiO_5 triple point: constraints from the Ballachulish aureole, Scotland. *Journal of Geology*, **100**, 423–446.

Pattison, D.R.M. & Harte, B., 1988. Evolution of structurally contrasting anatectic migmatites in the 3-kbar Ballachulish aureole, Scotland. *Journal of Metamorphic Geology*, **6**, 475–494.

Pattison, D.R.M. & Harte, B., 1991. Petrography and mineral chemistry of pelites. In: *Equilibrium and Kinetics in Contact Metamorphism: The Ballachulish Igneous Complex and its Aureole* (eds Voll, G., Topel, J., Pattison, D.R.M. & Seifert, F.), pp. 135–180. Springer Verlag, Heidelberg.

Pattison, D.R.M. & Harte, B., 1997. The geology and evolution of the Ballachulish Igneous Complex and Aureole. *Scottish Journal of Geology*, **33**, 1–29.

Pattison, D.R.M. & Tracy, R.J., 1991. Phase equilibria and thermobarometry of metapelites. In: *Contact Metamorphism* (ed. Kerrick, D.M.), *Mineralogical Society of America, Reviews in Mineralogy*, **26**, 105–206.

Pattison, D.R.M. & Vogl, J.J., 2005. Contrasting sequences of metapelitic mineral-assemblages in the aureole of the tilted Nelson Batholith, British Columbia: implications for phase equilibria and pressure determination in andalusite–sillimanite type settings. *Canadian Mineralogist*, **43**, 51–88.

Pattison, D.R.M., Spear, F.S., DeBuhr, C.L., Cheney, J.T. & Guidotti, C.V., 2002. Thermodynamic modelling of the reaction Muscovite + Cordierite = Al_2SiO_5 + Biotite + Quartz + H_2O: constraints from natural assemblages and implications for the metapelitic petrogenetic grid. *Journal of Metamorphic Geology*, **20**, 99–118.

Pattison, D.R.M., de Capitani, C. & Gaidies, F., 2011. Petrological consequences of variations in metamorphic reaction affinity. *Journal of Metamorphic Geology*, **29**, 953–977.

Reesor, J.E., 1973. Geology of the Lardeau Map-Area, East Half, British Columbia. *Geological Society of Canada Memoir*, **369**, 80–103.

Rutter, E.H., 1976. The kinetics of rock deformation by pressure solution. *Philosophical Transactions of the Royal Society of London, Series A: Mathematical and Physical Sciences*, **283**, 203–219.

Shimizu, I., 1995. Kinetics of pressure solution creep in quartz; theoretical considerations. In: *Influence of Fluids on Deformation Processes in Rocks* (eds Spiers, C.J. & Takeshita, T.), *Tectonophysics*, **245**, 121–134.

Spear, F.S., 1993. Metamorphic phase equilibria and pressure–temperature–time paths. *Mineralogical Society of America Monograph*, **1**, 799.

Spear, F.S. & Cheney, J.T., 1989. A petrogenetic grid for pelitic schists in the system $SiO_2–Al_2O_3–FeO–MgO–K_2O–H_2O$. *Contributions to Mineralogy and Petrology*, **101**, 149–164.

Spear, F.S. & Pyle, J.M., 2010. Theoretical modeling of monazite growth in a low-Ca pelite. *Chemical Geology*, **273**, 111–119.

Tinkham, D.K. & Ghent, E.D., 2005. Estimating P-T conditions of garnet growth with isochemical phase diagram sections and the problem of effective bulk-composition. *Canadian Mineralogist*, **43**, 35–50.

Tinkham, D.K., Zuluaga, C.A. & Stowell, H.H., 2001. Metapelite phase equilibria modeling in MnNCKFMASH: the effect of variable Al_2O_3 and MgO/(MgO+FeO) on mineral stability. *Mineralogical Society of America: Geological Materials Research*, **3**, 1–42.

Vernon, R.H., 1979. Formation of late sillimanite by hydrogen metasomatism (base-leaching) in some high-grade gneisses. *Lithos*, **12**, 143–152.

Waters, D.J. & Lovegrove, D.P., 2002. Assessing the extent of disequilibrium and overstepping of prograde metamorphic reactions in metapelites from the Bushveld Complex aureole, South Africa. *Journal of Metamorphic Geology*, **20**, 135–149.

White, R.W., Pomroy, N.E. & Powell, R., 2005. An in-situ metatexite–diatexite transition in upper amphibolite facies rocks from Broken Hill, Australia. *Journal of Metamorphic Geology*, **23**, 579–602.

White, R.W., Powell, R. & Holland, T.J.B., 2007. Progress relating to calculation of partial melting equilibria for metapelites. *Journal of Metamorphic Geology*, **25**, 511–527.

White, R.W., Powell, R., Holland, T.J.B., Johnson, T.E. & Green, C.R., 2014. New mineral activity–composition relations for thermodynamic calculations in metapelitic systems. *Journal of Metamorphic Geology*, **32,** 261–286.

SUPPORTING INFORMATION

Additional Supporting Information may be found in the online version of this article at the publisher's web site:

Figure S1. Map of lithology and structure, Cobalt Lake area.

Figure S2. Map of metamorphic mineral assemblages and isograds, Cobalt Lake area.

Figure S3. Structural cross-section, Cobalt Lake area.

Figure S4. Map of lithology and structure, Kickoff Meadows area.

Figure S5. Map of metamorphic mineral assemblages and isograds, Kickoff Meadows area.

Figure S6. Map of isograds, Iceberg Lake area.

Figure S7. Map of isograds, Bugaboo Glacier area.

Figure S8. Photographs and photomicrographs, Iceberg Lake and Bugaboo Glacier areas.

Table S1. Mineral assemblages in the Cobalt Lake, Kickoff Meadows, Iceberg Lake and Bugaboo Glacier areas of the Bugaboo aureole.

Table S2. Modes of mineral assemblages in Cobalt Lake area.

Table S3. Summary of key whole-rock and mineral chemical parameters from Cobalt Lake area.

Table S4. Whole-rock chemical analyses, Cobalt Lake area.

Table S5. Biotite analyses, Cobalt Lake area.

Table S6. Muscovite and paragonite analyses, Cobalt Lake area.

Table S7. Cordierite analyses, Cobalt Lake area.

Table S8. Andalusite analyses, Cobalt Lake area.

Table S9. Chlorite analyses, Cobalt Lake area.

Table S10. Plagioclase analyses, Cobalt Lake area.

Table S11. K-feldspar analyses, Cobalt Lake area.

Table S12. Ilmenite analyses, Cobalt Lake area.

Table S13. Whole-rock compositions of Bugaboo metapelites used for thermodynamic modelling.

Appendix S1. Compositional input file for Theriak/Domino used to calculate the phase diagrams in the paper.

Appendix S2. Thermodynamic input file for Theriak/Domino for Holland–Powell database 5.5 and the two sets of *a–x* models ('HP1' and 'HP2') described in the paper.

Appendix S3. Thermodynamic input file for Theriak/Domino for the SPaC14 database described in the paper.